Retrieval of the aerosol direct radiative effect over clouds from spaceborne spectrometry

M. de Graaf,[1] L. G. Tilstra,[1] P. Wang,[1] and P. Stammes[1]

Received 11 November 2011; revised 1 March 2012; accepted 5 March 2012; published 11 April 2012.

[1] The solar radiative absorption by an aerosol layer above clouds is quantified using passive satellite spectrometry from the ultraviolet (UV) to the shortwave infrared (SWIR). UV-absorbing aerosols have a strong signature that can be detected using UV reflectance measurements, even when above clouds. Since the aerosol extinction optical thickness decreases rapidly with increasing wavelength for biomass burning aerosols, the properties of the clouds below the aerosol layer can be retrieved in the SWIR, where aerosol extinction optical thickness is sufficiently small. Using radiative transfer computations, the contribution of the clouds to the reflected radiation can be modeled for the entire solar spectrum. In this way, cloud and aerosol effects can be separated for a scene with aerosols above clouds. Aerosol microphysical assumptions and retrievals are avoided by modeling only the pure (aerosol-free) cloud spectra. An algorithm was developed using the spaceborne spectrometer Scanning Imaging Absorption Spectrometer for Atmospheric Chartography (SCIAMACHY). The aerosol direct radiative effect (DRE) over clouds over the South Atlantic Ocean west of Africa, averaged through August 2006 was found to be 23 $\pm$ 8 Wm^{-2} with a mean variation over the region in this month of 22 Wm^{-2}. The largest aerosol DRE over clouds found in that month was 132 $\pm$ 8 Wm^{-2}. The algorithm can be applied to any instrument, or a combination of instruments, that measures UV, visible and SWIR reflectances at the top of the atmosphere (TOA) simultaneously.

Citation: de Graaf, M., L. G. Tilstra, P. Wang, and P. Stammes (2012), Retrieval of the aerosol direct radiative effect over clouds from spaceborne spectrometry, *J. Geophys. Res.*, *117*, D07207, doi:10.1029/2011JD017160.

1. Introduction

[2] The radiative effect of aerosols is one of the least certain components in global climate models [*Yu et al.*, 2006; *Forster et al.*, 2007]. This is mainly due to the aerosol influences on clouds. Aerosols can influence e.g., cloud formation, cloud albedo and cloud life time, through their role as cloud condensation nuclei, which are called the indirect effects of aerosols [e.g., *Haywood and Boucher*, 2000; *Lohmann and Feichter*, 2005]. But even the aerosol direct radiative effect (DRE), the component of aerosol radiative forcing that neglects all influences on clouds, is still poorly constrained, due to the heterogeneous distribution of aerosol sources and sinks and the influence of clouds on global observations of aerosols. In particular, the characterization of aerosol properties in cloudy scenes has proved challenging. Locally, the aerosol DRE can be very large and dominate the radiative forcing. Monitoring of the aerosol DRE from passive instruments with daily global coverage will be highly advantageous for the understanding of aerosol effects and the influence of aerosols on clouds.

[3] The aerosol DRE over clouds is studied most often in the southern African region, where annually recurring biomass burning events in the local dry season (June - September) produce light-absorbing aerosols that are advected over marine stratiform clouds [e.g., *Swap et al.*, 1996; *Herman et al.*, 1997; *Torres et al.*, 2002; *De Graaf et al.*, 2007]. Modeling studies of aerosol DRE differ in magnitude and sign, but all studies show that the DRE at the TOA strongly depends on the underlying surface. Over dark surfaces like the ocean, the scattering effects of the aerosols dominate, leading to a negative (cooling) DRE, while over bright surfaces and clouds aerosol absorption decreases the scene albedo, leading to a less negative or positive (warming) DRE [*Keil and Haywood*, 2003; *Abel et al.*, 2005; *Tummon et al.*, 2010]. The aerosol DRE over marine clouds was found to change sign from negative to positive at a geometric cloud fraction of 0.4 [*Chand et al.*, 2009]. These results depend on the diurnal cycle of clouds [e.g., *Myhre et al.*, 2003], while semi-direct effects change the results and can even dominate the DRE [*Sakaeda et al.*, 2011]. The semi-direct effect is strongest for absorbing aerosols inside the boundary layer, but still significant for aerosol layers that are located above the boundary layer [*Johnson et al.*, 2004].

[1]Climate Research and Seismology Department, Royal Netherlands Meteorological Institute, De Bilt, Netherlands.

0148-0227/12/2011JD017160

[4] Aerosol DRE shows a very strong dependence on aerosol microphysical properties. During the SAFARI 2000 field campaign, valuable information on scattering properties of biomass burning aerosols over clouds were obtained from air-borne measurements [*Haywood et al.*, 2003]. On a global basis the retrieval of aerosol properties in the presence of clouds is challenging. Most current satellite aerosol retrieval algorithms rely on cloud screening before retrieving aerosol information [e.g., *Torres et al.*, 1998; *Kahn et al.*, 1998; *Diner et al.*, 2001; *Hauser et al.*, 2005; *Remer et al.*, 2005]. Therefore, studies of the aerosol indirect effects from space-based instruments are necessarily often restricted to aerosols in the vicinity of clouds [e.g., *Redemann et al.*, 2009; *Costantino and Bréon*, 2010].

[5] In some cases cloud and aerosol information can be separated in the radiation received by satellite instruments at the TOA. UV-absorbing aerosols with an aerosol absorption optical thickness that decreases strongly with wavelength, like smoke, reduce the scene reflectance predominantly in the UV and visible spectral region, which may be used to retrieve the spectral optical aerosol properties in individual cases by fitting modeled reflectance spectra to the measured spectrum [*De Graaf et al.*, 2007]. However, the large number of aerosol properties determining the reflectance spectrum will often result in multiple solutions. The strong UV-absorption due to UV-absorbing aerosols over clouds may also be used to retrieve cloud optical thickness and aerosol optical thickness simultaneously, using precomputed tables of Absorbing Aerosol Index (AAI) versus cloud optical thickness [*Torres et al.*, 2011]. However, these retrievals are dependent on the correct selection of aerosol type. Aerosols also significantly affect the polarized light reflected by clouds under certain scattering geometries, which can be used to derive aerosol optical properties in cloudy scenes [*Waquet et al.*, 2009; *Knobelspiesse et al.*, 2011]. This can be used to derive aerosol DRE over clouds using spaceborne polarimetry measurements. In the case of active remote sensing, like lidar, the atmospheric scattering properties are vertically resolved, allowing for separation of aerosol and cloud properties in a small but global track [*Chand et al.*, 2008; *Wilcox*, 2010]. These aerosol microphysical and optical properties can be used to compute the aerosol DRE over clouds, but the accuracy of these results is strongly influenced by the accuracy of the aerosol parameters that are assumed to represent the actual aerosols.

[6] When aerosol vertical profiles are available, heating rates can be computed. Using various satellite cloud products and Ozone Monitoring Instrument (OMI) AAI [*Torres et al.*, 2007] as a proxy for aerosol presence, the liquid water path and geometric thickness of clouds were found to increase from the presence of aerosols above the clouds and the subsequent heating of the atmosphere [*Wilcox*, 2012]. This implies a negative semi-direct radiative effect of the aerosols. In another more statistical study the OMI AAI was found to decrease the local planetary albedo through the direct and first indirect effect, which allowed for the retrieval of the aerosol DRE in cloudy scenes in the tropical and subtropical oceans [*Peters et al.*, 2011].

[7] Over China, annually recurring rice straw burning also causes light-absorbing aerosols which are advected over the ocean and over clouds. The total upwelling shortwave flux as measured by Clouds and the Earth's Radiant Energy System (CERES) was found to be reduced by more than 100 Wm^{-2} over cloud scenes with high values of Total Ozone Mapping Spectrometer (TOMS) Aerosol Index (AI), indicating absorbing aerosol layers over the clouds [*Hsu et al.*, 2003].

[8] In this paper, we follow up on a technique to retrieve the aerosol DRE over clouds for biomass burning aerosols, using spectral reflectance observations from space [*Stammes et al.*, 2008], without the need of retrieving or assuming aerosol parameters. The UV-visible part of the reflectance spectrum is attenuated due to the light absorption by UV-absorbing aerosols, which results in a darkening of the scene in the UV. The SWIR part of the reflectance spectrum, however, is much less significantly attenuated by absorption due to biomass burning aerosols [*De Graaf et al.*, 2007]. Therefore, the cloud optical thickness τ_{cld} and cloud droplet effective radius r_{eff} can be retrieved in the part of the spectrum where the aerosol extinction optical thickness τ_{aer} has been reduced sufficiently. Using these and other parameters the cloud reflectance spectrum is modeled using a Radiative Transfer Model (RTM), thus effectively removing the aerosols from the scene. By comparison of the measured aerosol-polluted cloud scene and the modeled unpolluted cloud scene, the aerosol DRE can be estimated directly, without the need for any aerosol parameter estimates. This technique is illustrated here using the spaceborne spectrometer SCIAMACHY, which measures the shortwave reflectance spectrum contiguously from 240 to 1750 nm.

[9] The algorithm is formally derived in section 2. It relies on a number of readily available data products from satellite instruments, which are introduced in section 3. The simulation of aerosol-unpolluted cloud scenes is described in section 4. The derivation of the aerosol DRE over clouds is illustrated using SCIAMACHY measurements of scenes with biomass burning aerosols over marine boundary layer clouds on the South Atlantic Ocean in section 5. The accuracy of the derived DRE over clouds is estimated in section 6. Then, the regional monthly averaged aerosol DRE over the South Atlantic Ocean in August 2006 is derived and analyzed in section 7. Conclusions are drawn in section 8.

2. Theory

[10] The radiative effect of an atmospheric constituent can be defined as the net broadband irradiance change $\Delta\mathcal{E}$ at a certain level with and without the forcing constituent, after allowing for stratospheric temperatures to readjust to radiative equilibrium, but with tropospheric and surface temperatures and state held fixed at the unperturbed values [e.g., *Forster et al.*, 2007]. For tropospheric aerosols as the forcing agent, stratospheric adjustments have little effect on the radiative forcing and the instantaneous irradiance change at the TOA can be substituted:

$$\Delta\mathcal{E}_{\mathrm{aer}}^{\mathrm{TOA}} = \mathcal{E}_{\mathrm{with\ aer}}^{\mathrm{net}} - \mathcal{E}_{\mathrm{without\ aer}}^{\mathrm{net}}, \tag{1}$$

where $\mathcal{E}^{\mathrm{net}}$ is the net irradiance, defined as the difference between the downwelling and upwelling shortwave irradiances at the TOA, $\mathcal{E}^{\mathrm{net}} = \mathcal{E}^{\downarrow} - \mathcal{E}^{\uparrow}$. Furthermore, the extinction optical thickness of biomass burning aerosols decreases strongly with increasing wavelength. Therefore, biomass burning aerosols do not significantly interact with

the longwave (terrestrial) radiation, so the net broadband irradiance can be substituted by the net shortwave irradiance. At the TOA the shortwave downwelling irradiance is the total incoming solar irradiance $\mathcal{E}_0$ for any scene, and $\mathcal{E}^{\downarrow}$ can be eliminated. Consequently, for aerosols overlying a cloud the direct radiative effect is given by

$$\Delta\mathcal{E}_{\text{aer}}^{\text{TOA}} = \mathcal{E}_{\text{cld}}^{\uparrow\text{TOA}} - \mathcal{E}_{\text{cld+aer}}^{\uparrow\text{TOA}}, \tag{2}$$

where $\mathcal{E}_{\text{cld}}^{\uparrow\ \text{TOA}}$ is the upwelling irradiance at the TOA for an aerosol-unpolluted cloud scene and $\mathcal{E}_{\text{cld+aer}}^{\uparrow\ \text{TOA}}$ is the upwelling shortwave irradiance for an aerosol-polluted cloud scene. By equation (2), if energy is absorbed in the atmosphere by the aerosols, the direct radiative effect is positive.

[11] The primary product of SCIAMACHY is the Earth reflectance $R(\lambda)$, measured in the shortwave domain as a function of wavelength at a high spectral resolution (see section 3.1). The monochromatic reflectance $R(\lambda)$ is defined as the quotient of the upwelling monochromatic radiance $I(\lambda)$ and the downwelling monochromatic solar irradiance $E_0(\lambda)$:

$$R(\lambda) = \frac{\pi I(\lambda)}{\mu_0 E_0(\lambda)}, \tag{3}$$

where μ_0 is the cosine of the solar zenith angle θ_0 and $\mu_0 E_0$ is the solar irradiance incident on a horizontal surface unit at TOA. $R(\lambda)$ is also computed by the RTM at discrete wavelengths (see section 3.4). Below, R and all other quantities refer to the TOA.

[12] The monochromatic irradiance $E(\lambda)$ of the reflected radiation can be found by integrating $I(\lambda)$ over the entire hemisphere, weighted by μ, where μ is the cosine of the viewing zenith angle θ. Substituting equation (3) and using polar coordinates (θ, ϕ):

$$E(\lambda) = \frac{\mu_0 E_0(\lambda)}{\pi} \int_0^{2\pi}\int_0^1 R(\lambda;\mu,\phi;\mu_0,\phi_0)\mu\,\mathrm{d}\mu\mathrm{d}\phi, \tag{4}$$

where ϕ_0 and ϕ are the azimuth angles of the solar and viewing directions, respectively. Similarly, the (local) plane albedo A for a scene is defined as the integral of $R(\lambda)$ over the entire hemisphere [e.g., *Liou*, 2002]:

$$A(\lambda,\mu_0) = \frac{1}{\pi}\int_0^{2\pi}\int_0^1 R(\lambda;\mu,\phi;\mu_0,\phi_0)\mu\,\mathrm{d}\mu\mathrm{d}\phi. \tag{5}$$

By substituting equation (5) in (4) and integrating over wavelength in the shortwave (SW) domain, equation (2) becomes

$$\Delta\mathcal{E}_{\text{aer}} = \int_{\text{SW}} \mu_0 E_0 (A_{\text{cld}} - A_{\text{cld+aer}})\mathrm{d}\lambda. \tag{6}$$

Here we have omitted the wavelength and solar zenith angle dependence of the terms on the right hand side.

[13] In this paper the aerosol DRE over clouds is determined using RTM results for the first term in equation (6), A_{cld}, and measurements of the reflectance $R(\lambda)$ from SCIAMACHY for the second term, $A_{\text{cld+aer}}$. From the RTM results, the plane albedo A_{cld} can be determined from integration of the reflectances in all directions. However, from SCIAMACHY only the reflectance in the viewing direction is known. Therefore, the plane albedo for this scene, $A_{\text{cld+aer}}$, must be estimated. A measure for the angular distribution of the reflected radiation for a scene is the anisotropy factor $B(\lambda,\ \mu_0) = R/A$. The anisotropy factors are assumed to be equal for the aerosol-unpolluted and aerosol-polluted cloud scenes, $B_{\text{cld}} = B_{\text{cld+aer}}$. Furthermore, the wavelength integration limits are 240 and 1750 nm, the range of SCIAMACHY contiguous reflectance measurements. Then, equation (6) can be written as

$$\Delta\mathcal{E}_{\text{aer}} = \int_{240\,\text{nm}}^{1750\,\text{nm}} \frac{\mu_0 E_0 (R_{\text{cld}} - R_{\text{cld+aer}})}{B_{\text{cld}}}\mathrm{d}\lambda + \epsilon, \tag{7}$$

where ϵ is the error in the algorithm, due to the assumptions described above and the measurement uncertainties. These will be quantified in section 6. Equation (7) is used to derive the aerosol DRE over clouds from SCIAMACHY measurements of $R_{\text{cld+aer}}$ and RTM results of R_{cld} and B_{cld}.

3. Data

[14] In this section satellite data products are discussed briefly that are used throughout the paper, but have been derived and described elsewhere.

3.1. SCIAMACHY

[15] SCIAMACHY is part of the payload of the European Space Agency's Environmental Satellite (Envisat), launched on 1 March 2002 into a polar orbit at about 800 km altitude, with an equator crossing-time of 10:00 a.m. (local time) for the descending node, orbiting the Earth every 100 min. SCIAMACHY is a spectrometer designed to measure sunlight, reflected by the Earth's atmosphere and surface, in eight channels from 240 to 2380 nm at a spectral resolution of 0.2 – 1.5 nm [*Bovensmann et al.*, 1999].

3.1.1. Reflectance Measurements

[16] SCIAMACHY observes the radiance in two alternating modes, nadir and limb, yielding data blocks called states. The size of a typical nadir state is approximately 960 × 490 km^2. In nadir mode, SCIAMACHY scans the Earth from east to west in four seconds by rotating one of its internal mirrors. The size of the nadir footprints is proportional to the internal integration time (IT). Radiance measurements are available at different ITs for different parts of the spectrum, varying with location. Typical footprints relevant in this study are 60 × 30 km^2 (IT = 0.25 s) and 240 × 30 km^2 (IT = 1 s). However, by co-adding pixels a contiguous reflectance spectrum from 240–1750 nm can always be obtained for a 1 s IT. For this study, contiguous 0.25 s IT reflectance spectra were created by interpolation of the 1 s IT spectrum in the missing parts of the 0.25 s IT spectrum.

[17] Once per day SCIAMACHY measures the solar irradiance for radiometric calibration purposes. Changes in the instrument's throughput are monitored by observing the Sun via internal light paths that are assumed to be representative for the actual internal light paths in the nadir or limb measurement mode. Changes in this throughput are

monitored to describe and correct for the degradation of the individual light paths [e.g., *Noël et al.*, 2007; *Bramstedt et al.*, 2009]. SCIAMACHY's reflectances have been validated using satellite intercomparisons [e.g., *Acarreta and Stammes*, 2005; *Jourdan et al.*, 2005; *von Hoyningen-Huene et al.*, 2007; *Tilstra et al.*, 2012] and RTM calculations [*Tilstra et al.*, 2005; *van Soest et al.*, 2005]. The latter are important, because RTM results are used here to simulate the aerosol-unpolluted cloud reflectance spectra, which are compared to the measured reflectance spectra. A comparison of measured and modeled aerosol-unpolluted cloud reflectance spectra will be used in section 6 to estimate the accuracy of the modeled aerosol-unpolluted cloud reflectance spectra, providing an independent validation of the SCIAMACHY reflectance calibration over the entire domain.

[18] The required solar irradiance spectrum $E_0(\lambda)$ in equation (7) is taken from *Gueymard* [2004].

3.1.2. FRESCO Cloud Pressure and Fraction

[19] Cloud pressure and cloud fraction are retrieved using the Fast Retrieval Scheme for Clouds from the Oxygen A-band (FRESCO) applied to SCIAMACHY measurements [*Wang et al.*, 2008]. FRESCO retrieves cloud pressure (CP) and effective cloud fraction (CF) by fitting the measured reflectance in and around the O_2-A absorption band at 760 nm with modeled reflectances for scenes with different cloud fractions and cloud pressures. The cloud albedo in the retrieval is fixed to 0.8, therefore CF differs from the geometric cloud fraction. However, CF is well suited to describe the reflectance from a partly cloudy scene, because the reflectance is constant for a constant CF (and constant surface albedo), even if the actual geometrical cloud fraction and cloud optical thickness may vary. The FRESCO CF is used to select scenes with sufficient amounts of clouds in the scene. The sensitivity of FRESCO retrievals to overlying aerosol layers is assessed in section 6.2.3.

[20] The depth of the O_2 A-band is proportional to the oxygen column above the surface or cloud, which is used to determine the height of a cloud. FRESCO cloud pressure is close to the optical mid-level of the cloud [*Wang et al.*, 2008]. The sensitivity of cloud pressure retrievals, from various instruments and algorithms, to absorbing aerosol layers was shown using 'Polarization and Anisotropy of Reflectances for Atmospheric Science coupled with Observations from a Lidar' (PARASOL) observations, for a case with an absorbing aerosol layer (fine-mode fraction AOT < 0.3) located between 2 and 4 km above low-level clouds at around 1 km altitude (determined from CALIOP measurements) [*Waquet et al.*, 2009]. Cloud-top pressure retrievals based on the use of spectral polarized radiance measurements [*Goloub et al.*, 1994] were shown to be severely affected by the aerosol layer, with up to 700 hPa smaller values as compared to CALIOP cloud-top pressure. Cloud-top pressure determined from MODIS thermal infrared (THIR) measurements [*Menzel et al.*, 2006] was about 100 hPa lower than the CALIOP cloud-top pressure, which may be due to the presence of the aerosol layer or differences in the algorithms. On the other hand, the O_2 A-band cloud pressure was consistently close to the CALIOP cloud pressure for both aerosol-unpolluted and aerosol-polluted cloud scenes. Therefore, in this paper FRESCO CP is used to determine the height of the clouds.

3.1.3. Cloud Thermodynamic Phase

[21] The thermodynamic phase of a cloud in a scene can be determined using the Cloud Phase Index (CPI) [*Knap et al.*, 2002; *Acarreta et al.*, 2004]. The CPI is a measure of the slope of the reflectance spectrum between 1640 and 1700 nm, by which ice and water clouds can be discriminated. Because the aerosol extinction optical thickness of smoke is very small at these wavelengths, smoke layers will not affect the index. In this paper, ice clouds are filtered using the CPI to avoid retrieval errors.

3.1.4. Absorbing Aerosol Index

[22] Aerosol absorption in the UV, typically caused by smoke, desert dust, and volcanic ash particles, can be identified using the AAI [*Herman et al.*, 1997; *Torres et al.*, 1998; *De Graaf et al.*, 2005]. The SCIAMACHY AAI is retrieved in the UV from the 340 and 380 nm wavelength pair [*De Graaf and Stammes*, 2005; *Tilstra et al.*, 2012]. Positive values of the AAI are indicative of UV-absorbing aerosols, in both cloudy and cloud-free scenes. When a cloud is present under an aerosol layer, the AAI value is increased, because the cloud acts as a bright elevated background [*De Graaf et al.*, 2005]. Furthermore, the absolute value of the AAI can change for different geometries and cloud-aerosol configurations, and aerosol properties and aerosol DRE cannot quantitatively be derived from it. However, the AAI has proved an excellent proxy to find aerosol-polluted cloud scenes when combined with cloud fraction data [*Stammes et al.*, 2008; *Peters et al.*, 2011; *Wilcox*, 2012]. The AAI can be used to select cloud scenes with (AAI > 1) and without absorbing aerosols (AAI < 0).

3.1.5. TOSOMI Ozone

[23] Ozone absorption in the Chappuis band (UV-visible) modulates the reflectance spectrum, which must be incorporated in the RTM to model the cloud reflectance spectrum correctly. The total ozone column used in this paper is retrieved from the 325–335 nm wavelength window, using the SCIAMACHY TOSOMI algorithm [*Eskes et al.*, 2005]. Aerosol layers may affect the retrieved ozone column through errors in the slant column. Aerosol scattering effects are implicitly corrected for by the cloud correction scheme. Aerosol absorption effects in total ozone are expected to be <1%, except when aerosol load is extremely heavy ($\tau > 3$) [*Bhartia*, 2002; *Veefkind et al.*, 2006]. These aerosol effects on the total ozone column will have a negligible effect on the retrieved aerosol DRE, as will be shown in section 4.2.

3.2. MERIS RGB

[24] The MEdium Resolution Imaging Spectrometer (MERIS) on-board Envisat is an imager with fifteen channels in the solar spectral range [*Rast and Bezy*, 1999], which provides excellent collocation with SCIAMACHY measurements. Its RGB images are used in this paper for visual verification of the horizontal distribution of clouds.

3.3. CALIOP

[25] The Cloud-Aerosol Lidar with Orthogonal Polarization (CALIOP) is part of the CALIPSO satellite payload, which was launched on 28 April 2006 and flies in the A-train constellation [*Stephens et al.*, 2002]. The CALIOP laser transmits linearly polarized light at 532 and 1064 nm at a pulse rate of 20.16 Hz. The backscatter intensity is received at 532 and 1064 nm, with the first divided into two

Table 1. Spectral Cloud Reflectance Lookup Table Nodes

Parameter	Nodes
Wavelength λ (nm)	295, 310, 340, 380, 430, 610, 867, 1051, 1246, 1640
Cloud optical thickness τ_{cld}	2, 4, 8, 12, 16, 20, 24, 32, 48
Droplet size r_{eff} (μm)	3, 4, 6, 8, 12, 16, 20, 24
Cloud base height z_{cld} (km)	0, 1, 4, 8, 12
Total O_3 column Ω (DU)	267, 334, 401
Surface albedo A_s	0, 0.5, 1
Droplet size eff. variance ν_{eff}	0.15
Number of θ_0, θ, $\phi - \phi_0$	36, 36, 19

orthogonally polarized components [e.g., *Winker et al.*, 2007]. The backscatter intensity measurements are used in this paper to show the vertical separation of clouds and aerosols.

3.4. Radiative Transfer Model

[26] The Doubling-Adding KNMI (DAK) RTM [*Stammes*, 2001] was used for the simulations of the reflectances. DAK computes the vectorized monochromatic reflectance and transmittance of a pseudo-spherical atmosphere, using the polarized doubling-adding method [*De Haan et al.*, 1987]. The internal radiation field of the atmosphere is determined in a finite number of layers, each of which can have Rayleigh scattering, gas absorption, and aerosol and cloud particle scattering and absorption.

4. Algorithm Description

[27] The aerosol DRE over clouds can be derived using a SCIAMACHY measured reflectance spectrum of an aerosol-polluted cloud scene and the modeled reflectance spectrum of the equivalent aerosol-unpolluted cloud scene; see equation (7). In order to model the reflectance spectrum of the unpolluted cloud scene, a lookup table (LUT) was created of reflectances at wavelengths outside the major gas absorption bands, for a range of cloud parameters.

4.1. Unpolluted Cloud Reflectance LUT

[28] A reflectance LUT at several wavelengths in the shortwave range was created for scenes with water clouds under various conditions. The wavelengths and the nodes of the LUT are listed in Table 1. Only water clouds were modeled, which are the most likely ones encountered when aerosols overlie the cloud. The geometrical thickness of the cloud was one kilometer. The scattering by water droplets was simulated using Mie scattering [*De Rooij and van der Stap*, 1984]. A gamma-distribution with effective radii r_{eff} varying between 3 and 24 μm was used, with an effective variance ν_{eff} of 0.15. This value is between typical values for stratus and stratocumulus clouds [*Hansen*, 1971]. The cloud optical thickness τ_{cld} was varied from 2 to 48. The atmosphere was divided into 32 layers and a standard midlatitude atmosphere gas and temperature profile was used [*Anderson et al.*, 1986], with a surface pressure of 1013 hPa. To account for ozone column variations, three different ozone column values were used. Linear interpolation is used for all parameters described above.

[29] To account for surface albedo, three surface albedo nodes suffice in the LUT, if the surface is assumed to be Lambertian. In that case the contribution to the reflectance from the atmosphere and the surface can be separated [cf. *Chandrasekhar*, 1960; *De Graaf et al.*, 2005] and the surface albedo can be treated analytically.

4.2. Cloud Reflectance Sensitivity

[30] In order to simulate the unpolluted cloud reflectance spectrum, an aerosol-polluted cloud reflectance spectrum measurement from SCIAMACHY is analyzed and the various scene and cloud parameters are retrieved or prescribed. The sensitivity of the simulated cloud reflectance and the retrieved aerosol DRE to the various input parameters can be determined from the LUT. Figure 1 shows the dependence of water cloud reflectances on various parameters for a few relevant wavelengths. It shows that cloud reflectances are mainly determined by cloud optical thickness τ_{cld} at all wavelengths and cloud droplet effective radius r_{eff} in the SWIR (Figure 1a). Cloud height has a small impact on the cloud reflectance (Figure 1b). The surface albedo is important at all wavelengths, especially for small cloud optical thickness (Figure 1c), which is relevant in combination with cloud fraction. The influence of ozone is very small in ozone absorption bands, shown by the 330 and 610 nm reflectances, and absent outside ozone absorption bands (Figure 1d).

4.2.1. Cloud Optical Thickness and Droplet Effective Radius

[31] The dependence of the reflectance of water clouds on cloud optical thickness τ_{cld} and cloud droplet effective radius r_{eff} as shown in Figure 1a can be used to retrieve τ_{cld} and r_{eff} using the measured spectral reflectances. The cloud reflectance for wavelengths below 1000 nm is mainly determined by the optical thickness of the cloud, while the cloud reflectance for wavelengths above about 2500 nm is mainly determined by droplet size [*Nakajima and King*, 1990]. Between these two wavelengths the reflectance carries information of both parameters. This is the basis for the simultaneous retrieval of r_{eff} and τ_{cld} using reflectances at two wavelengths in the indicated ranges. This method is used by, e.g., Advanced Very High Resolution Radiometer (AVHRR) [*Kawamoto et al.*, 2001], Moderate Resolution Imaging Spectroradiometer (MODIS) [*Platnick et al.*, 2003], Spinning Enhanced Visible and Infrared Imager (SEVIRI) [*Roebeling et al.*, 2006] and SCIAMACHY [*Kokhanovsky et al.*, 2005]. For wavelengths below about 1000 nm, however, the optical thickness of absorbing aerosols is not negligible in many cases, and the reflectance can be attenuated by aerosol absorption. Consequently, r_{eff} and τ_{cld} can be significantly perturbed by overlying aerosol layers [*Haywood et al.*, 2004; *Coddington et al.*, 2010]. This effect increases with increasing aerosol (absorption) optical thickness. Since the aerosol-unpolluted cloud reflectance is very sensitive to changes in τ_{cld} and r_{eff}, as Figure 1a shows, the cloud parameters must be retrieved at wavelengths in the SWIR where the aerosol absorption optical thickness is sufficiently small [*De Graaf et al.*, 2007].

[32] An algorithm, similar to the ones mentioned above, was developed here to retrieve r_{eff} and τ_{cld} from SCIAMACHY SWIR reflectances, using a subset of the LUT described in section 4.1. Three wavelengths in the SWIR were used, around 1051, 1246 and 1640 nm, while the 867 nm reflectance was used to verify the algorithm with the MODIS/SEVIRI Cloud

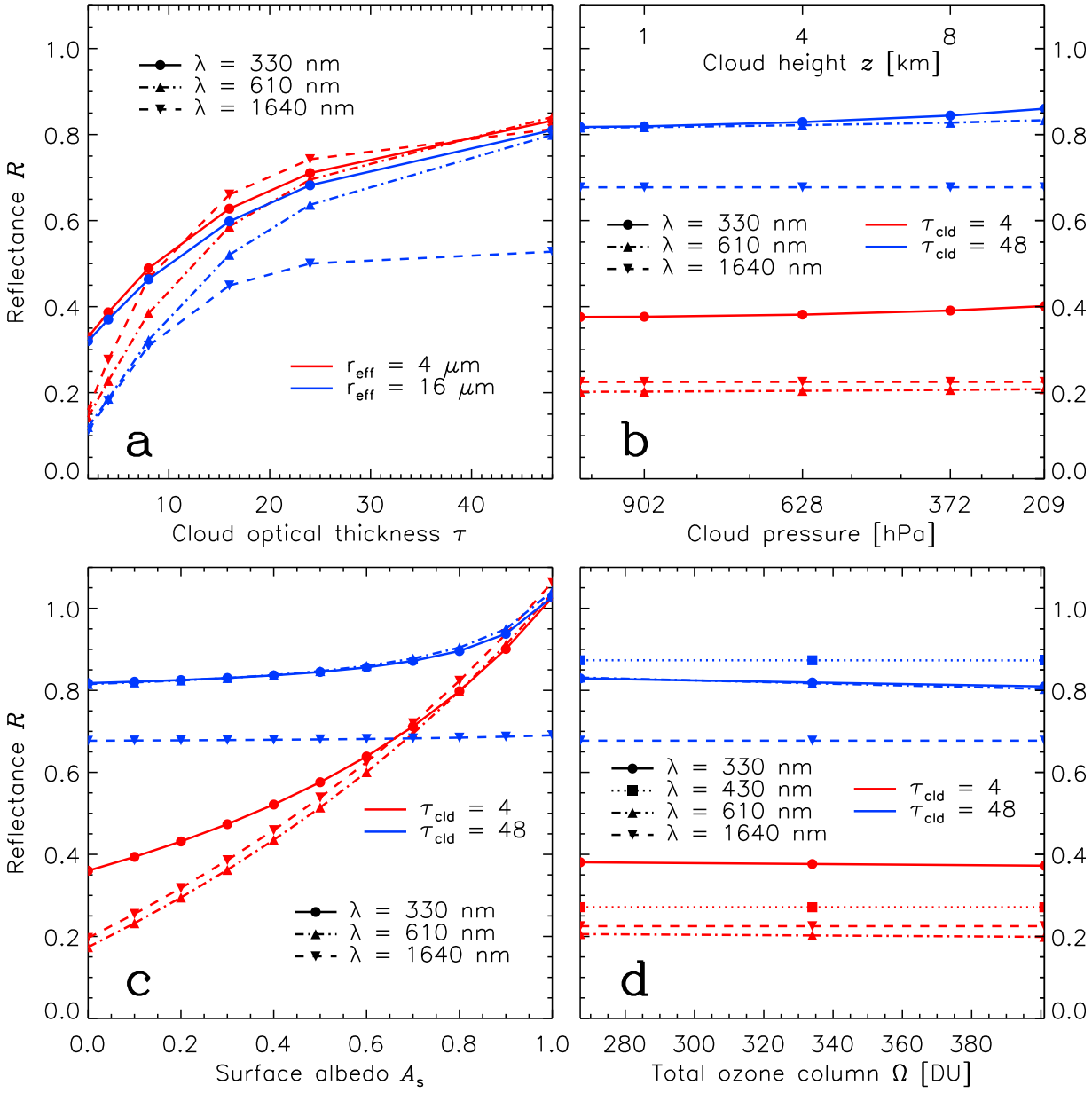

Figure 1. Sensitivities of the simulated aerosol-unpolluted cloud reflectances for various model input parameters shown at a selection of wavelengths: (a) sensitivity to cloud optical thickness τ for small (4 μm) and large (16 μm) droplets; (b) sensitivity to cloud pressure for thin (τ = 4) and thick (τ = 48) clouds; (c) sensitivity to surface albedo for thin and thick clouds; (d) sensitivity to total ozone column Ω for thin and thick clouds for wavelengths inside (330 and 610 nm) and outside (430 and 1640 nm) ozone absorption bands. Standard model parameters were: surface albedo A_s = 0.05, total ozone column Ω = 334 DU, cloud fraction CF = 1, cloud pressure CP = 902 hPa, cloud droplet effective radius r_{eff} = 8 μm, scattering geometry [θ, θ_0, $\phi - \phi_0$] = [0°, 20°, 0°], except where varied as indicated in the panels.

Physical Properties (CPP) retrieval algorithm (J. F. Meirink, personal communication, 2011). The 1640 nm reflectance is used as the higher wavelength at which to retrieve the cloud parameters. Both the 1051 nm and 1246 nm reflectances can be used together with the 1640 nm reflectance to retrieve the cloud parameters. At 1051 nm the residual τ_{aer} will have the largest impact, while at 1246 nm the retrieval of r_{eff} and τ_{cld} will be more sensitive to reflectance measurement errors. In this paper, the 1246 nm reflectance was used to minimize the effect of residual τ_{aer} in strongly aerosol-polluted cloud scenes. An estimate of the uncertainty introduced due to residual τ_{aer} at this wavelength and the measurement uncertainty is given in section 6.2.2.

4.2.2. Cloud Pressure

[33] The dependence of the cloud reflectance on cloud pressure is small (Figure 1b). The cloud reflectance depends on cloud pressure only in the UV. A variation in cloud pressure of 200 hPa induces a variation of less than 1% in

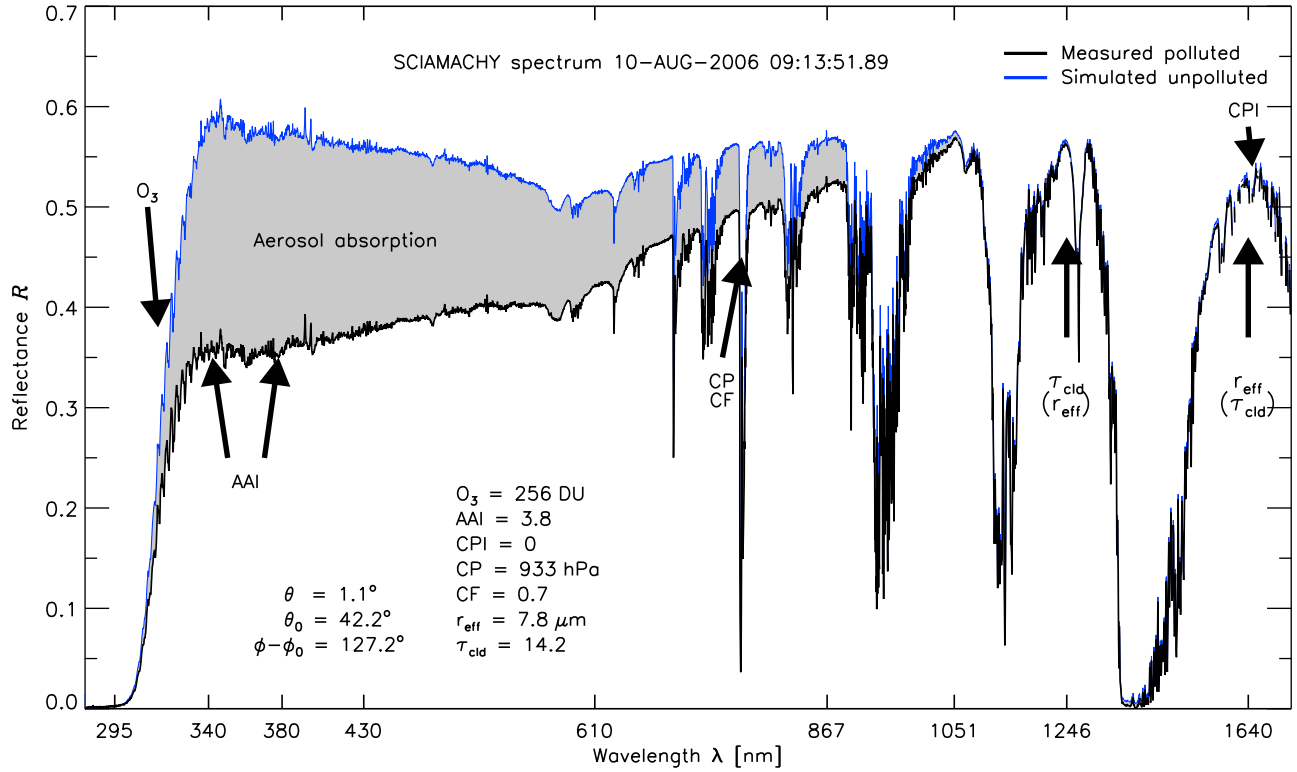

Figure 2. SCIAMACHY measured aerosol-polluted cloud reflectance spectrum (black) and equivalent modeled aerosol-unpolluted cloud reflectance spectrum (blue) of 10 August 2006 at 09:13:51.89 UTC. The difference between the measured and simulated cloud reflectance is caused by aerosol absorption, indicated by the gray shaded area. The scene was characterized by a high AAI of 3.8, indicating the presence of absorbing aerosols. The cloud phase index CPI was 0, the FRESCO cloud fraction CF was 0.7 and the cloud pressure CP 933 hPa, indicating a closed deck of low level (marine) water clouds. The retrieved cloud optical thickness τ_{cld} for this scene was 14.2, with an effective droplet size r_{eff} of 7.8 μm.

cloud reflectance in the UV [*Ahmad et al.*, 2004]. The dependence of FRESCO CP on absorption of overlying aerosol layers is quantified in section 6.2.3.

4.2.3. Cloud Fraction and Surface Albedo

[34] Small variations in cloud fraction can have a large impact on the simulated cloud reflectance due to the potentially large influence of the surface albedo, see Figure 1c. Therefore, in this paper only ocean scenes are considered, which generally have low surface reflectivities in the order of a few percent, especially at visible and SWIR wavelengths [*Koelemeijer et al.*, 2003]. In our model, a spectral surface albedo for all ocean scenes is assumed, ranging from 0.05 in the UV and decreasing to 0.025 in the SWIR. If the surface reflectivity is small and the scene contains enough clouds, the cloud-free (Rayleigh) reflectance R_{Rayl} is small compared to the cloud reflectance R_{cld}. In that case it is sufficient to model the cloud reflectance only. Scenes with FRESCO CF > 0.3 are used only, to ensure the presence of enough clouds in the scenes.

4.2.4. Gas Absorption

[35] The influence of ozone variations on the modeled cloud reflectance is small, as shown by Figure 1d. The same is true for possible variations in other gases, because only specific absorption lines are potentially affected. Therefore, the SCIAMACHY measured cloud spectrum can be used to fill in the spectrum between the tabulated wavelengths to simulate the fine structured absorption bands in the unpolluted cloud reflectance spectrum. The aerosols can be assumed to have a negligible influence on the gas absorption lines in the spectrum. This was tested by changing (decreasing) all absorption lines by the same amount as the continuum was decreased due to the presence of absorbing aerosols. This increased the retrieved aerosol DRE over clouds by less than 1 Wm^{-2} for all cases, because the absorption lines contribute little to the integral.

5. Application to SCIAMACHY

5.1. Spectrally Resolved Aerosol DRE Over Clouds

[36] The algorithm described in section 4 is illustrated in Figure 2. The SCIAMACHY reflectance spectrum observed on 10 August 2006, 09:13:51.89 UTC is shown in black. This is a typical measurement of a scene with smoke from the African continent that was advected over a marine low level cloud layer. The geometry for this scene was $[\theta, \theta_0, \phi - \phi_0] = [1.1°, 42.2°, 127.2°]$. The total ozone column from the TOSOMI algorithm was 256 DU. The FRESCO cloud pressure and cloud fraction were 933 hPa and 0.7, respectively. The cloud droplet effective radius and cloud optical thickness, retrieved from the SWIR, were 7.8 μm and 14.2, respectively. With these parameters an aerosol-unpolluted cloud reflectance spectrum was modeled,

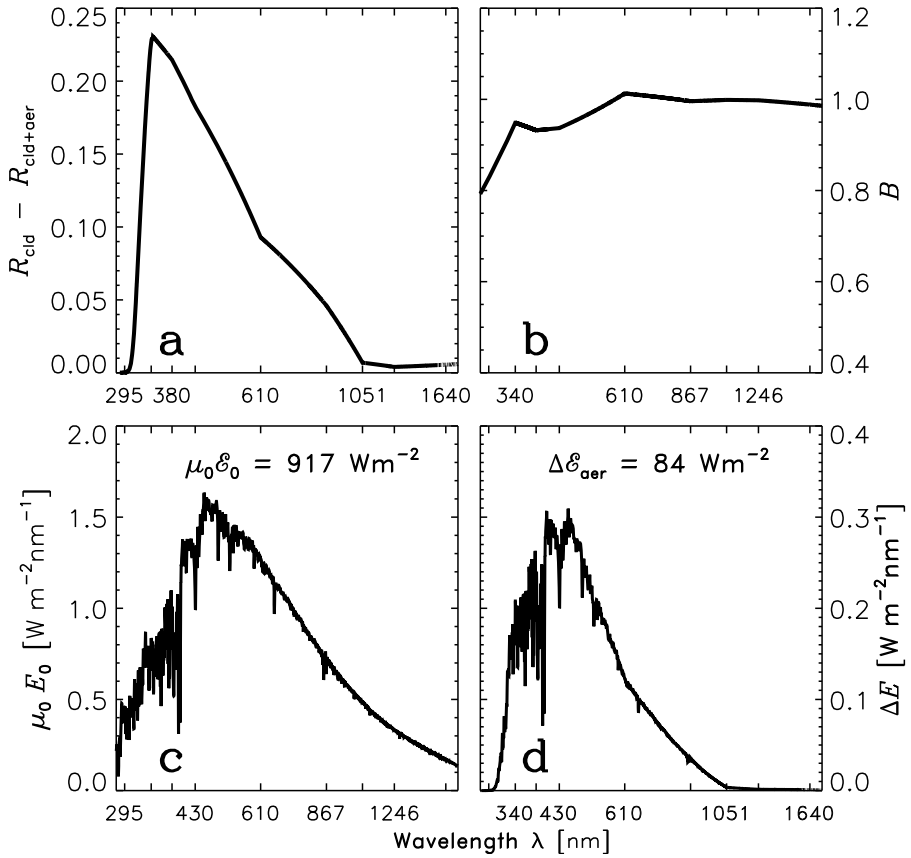

Figure 3. The various terms of equation (7) to determine the aerosol DRE over clouds for the scene in Figure 2, as a function of wavelength in the SCIAMACHY spectral range. (a) The reflectance difference $R_{cld} - R_{cld+aer}$ between the modeled aerosol-unpolluted and the measured aerosol-polluted cloud scene (same as shaded area in Figure 2); (b) The anisotropy factor of the modeled aerosol-unpolluted cloud scene; (c) The incoming solar irradiance at TOA; (d) The net irradiance change, i.e. the aerosol DRE.

which is indicated by the blue curve. The measured and modeled spectra are close for wavelengths longer than 1246 nm, due to the assumption that the aerosol absorption optical thickness is negligible at these wavelengths. At wavelengths shorter than about 1100 nm, the reflectance spectra start to deviate, which is indicated by the shaded gray area. The difference increases with decreasing wavelength. This is caused by the aerosol absorption optical thickness, which increases with decreasing wavelength. At wavelengths below about 300 nm the differences disappear, because there the reflectance of the scene becomes zero due to ozone absorption. The aerosol absorption in the scene is confirmed by the high value of the AAI of 3.8.

[37] The aerosol DRE over clouds for this scene was evaluated using equation (7). The various terms of this equation for the scene shown in Figure 2 are given in Figure 3 as a function of wavelength in the SCIAMACHY spectral range. The reflectance difference ($R_{cld} - R_{cld+aer}$) is given in Figure 3a, which is the same as the shaded gray area in Figure 2. It decreases with wavelength, except at those UV wavelengths where ozone absorption is so dominant that all radiation is absorbed. This term contains all the absorption effects in the scene which are not incorporated in the modeled cloud scene, and which are attributed to aerosol absorption. The anisotropy factor for the modeled cloud scene B_{cld} is plotted in Figure 3b; it is typically 0.8–1.0. The anisotropy factor for the aerosol-polluted cloud scene is not known, but in section 6.2.1 an estimate is given by modeling also the aerosol-polluted cloud scene. The solar irradiance at TOA $\mu_0 E_0$ is given in Figure 3c. The total incident solar irradiance from 240–1750 nm can be obtained by integrating the given irradiance spectrum and was 917 Wm^{-2}. The spectral irradiance change due to aerosol absorption ($E_{cld} - E_{cld+aer}$) can be obtained by combining these three terms according to equation (7), and is plotted in Figure 3d. By integrating over wavelength the total aerosol DRE over clouds $\Delta\mathcal{E}_{aer}$ was found to be 84 Wm^{-2} for this scene. Note that the spectral range of SCIAMACHY covers 92% of the solar energy spectrum, which is sufficient to capture the entire spectral aerosol DRE over clouds. The aerosol DRE becomes zero due to ozone absorption of the radiation below 300 nm and it also becomes zero for wavelengths longer than 1246 nm, assuming that the aerosol absorption has become negligible around that wavelength. The integration over SCIAMACHY's spectral range does not introduce an additional error as long as the aerosol absorption has become negligible around 1750 nm.

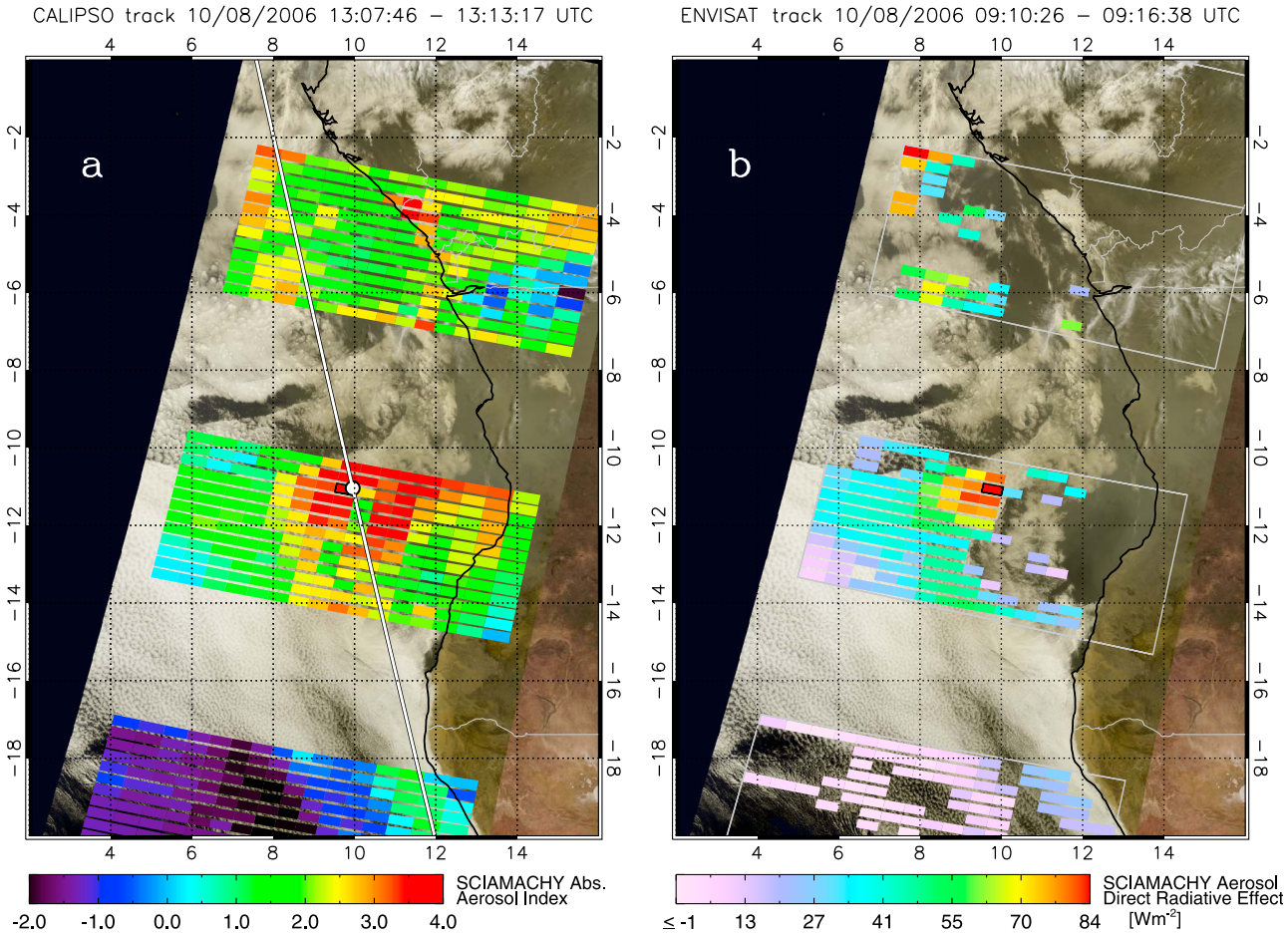

Figure 4. (a) Smoke pollution from central-west Africa over clouds on the South Atlantic Ocean, shown by MERIS RGB imagery on 10 August 2006 from 09:10:26 – 09:16:38 UTC, overlaid with SCIAMACHY AAI values (same time). The MERIS and SCIAMACHY images were acquired from North to South (descending orbit of Envisat). Also overlaid is the path of the CALIPSO track on the same day from 13:07:46 – 13:13:17 UTC as the white line. The CALIPSO daytime track is from South to North (ascending). The white dot on the CALIPSO track corresponds with the red arrow in Figure 5. The spectrum of the 0.25 s pixel indicated by the black rectangle is shown in Figure 2. (b) Same MERIS RGB image as Figure 4a, overlaid with aerosol DRE for marine water cloud scenes with CPI < 5 and CF > 0.3.

5.2. Horizontal Distribution of Aerosol DRE Over Clouds

[38] The algorithm can be applied to any ocean scene that contains water clouds. This is illustrated in Figure 4. In August 2006 a two-week period of high AAI over clouds was observed over the South Atlantic Ocean off the west coast of Namibia. These events can often be observed in this area from June to September, which is the local dry season. The high AAI values are caused by smoke from vegetation fires on the African mainland, which are advected over the Atlantic at altitudes of typically 1–5 km [e.g., *Herman et al.*, 1997; *Torres et al.*, 2002; *De Graaf et al.*, 2007].

[39] A typical horizontal distribution of the cloud and aerosol fields off the west coast of Namibia is shown in Figure 4a, where SCIAMACHY AAI measurements are overlaid on a MERIS RGB image. Clearly, the horizontal distributions of aerosols and clouds are very variable. Furthermore, they change rapidly from day to day.

[40] The corresponding aerosol DRE field over marine clouds is shown in Figure 4b, for all scenes over the ocean containing water clouds (CPI < 5) with effective cloud fractions greater than 0.3. It shows the unprecedented details of measured absorbed energy by aerosols over clouds. Clearly, the aerosol DRE is highly variable with location, dropping off to zero at the edges of the smoke field, which corresponds to the AAI gradient. The maximum aerosol DRE over clouds measured by SCIAMACHY on this day is 84 Wm^{-2}, indicated by the black rectangle. The measured reflectance spectrum for this scene was given in Figure 2. The minimum DRE was less than 0, which is not an indication of a negative aerosol DRE, but caused by the uncertainty of the measurements. The scale is cut at -1 Wm^{-2}, indicating that the aerosol DRE has vanished and aerosol-unpolluted clouds remain. The measurement uncertainty will be estimated in the next section.

[41] The vertical configuration for the event in Figure 4 is shown using a spatially collocated CALIPSO overpass. The

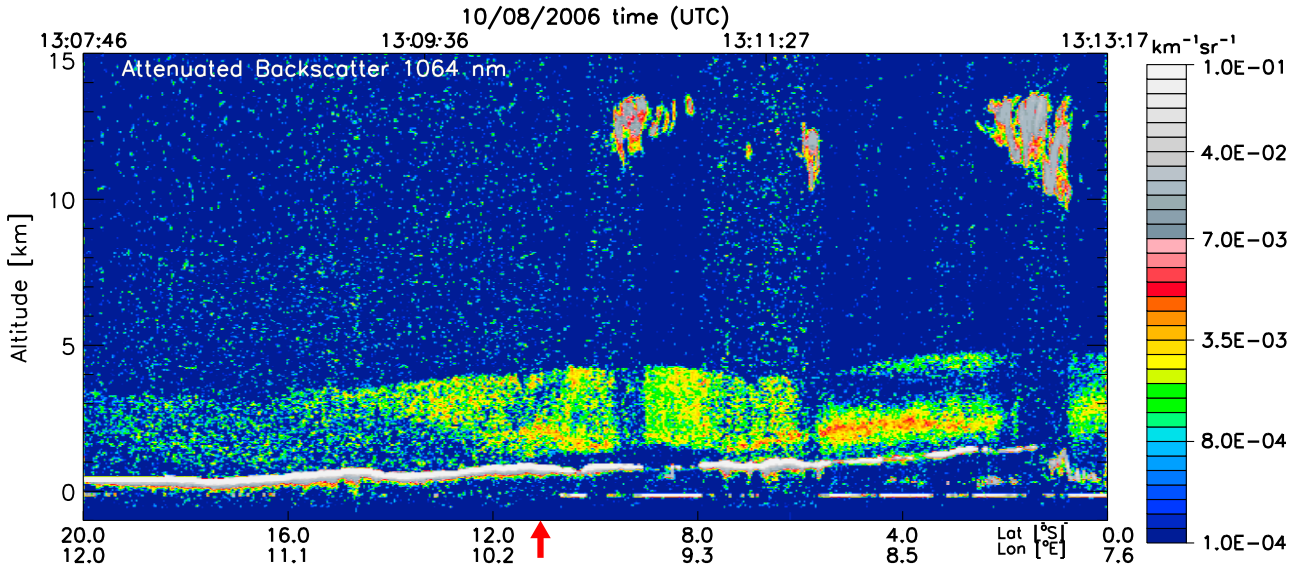

Figure 5. Smoothed daytime CALIPSO 1064 nm attenuated backscatter signal, showing the vertical aerosol and cloud layer distribution on 10 August 2006 from 13:07:46 – 13:13:17 UTC, between −0.5 and 15 km altitude, along the track indicated in Figure 4. The color scale is such that gray to white colors indicate clouds, green to yellow/red colors indicate aerosol layers and blue to green colors indicate background with noise. The red arrow indicates the location of the white dot in Figure 4.

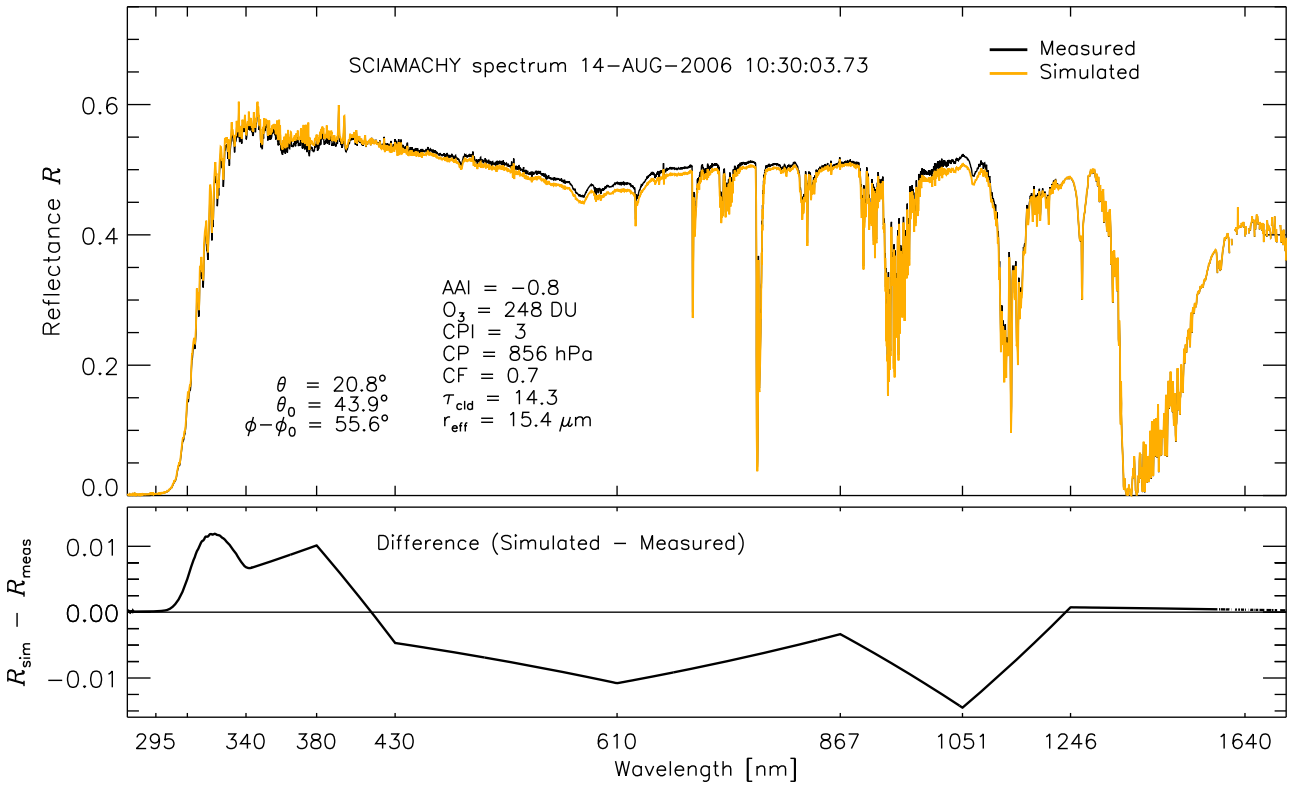

Figure 6. (top) Simulated (orange) and measured (black) reflectance spectra of an aerosol-unpolluted water cloud scene on 14 August 2006 at 10:30:03.73 UTC. The absence of absorbing aerosols above the clouds was ensured by the negative value of the AAI of −0.8. This scene was characterized by a cloud phase index of 3, a cloud fraction of 0.7 and a cloud pressure of 856 hPa, indicating a low level marine cloud. The retrieved τ_{cld} for this scene was 14.3, the r_{eff} was 15.4 μm. The simulated cloud spectrum for these cloud parameters, the scene geometry and a total ozone column of 248 DU, is shown in orange. (bottom) The reflectance difference between the simulated and measured cloud scene.

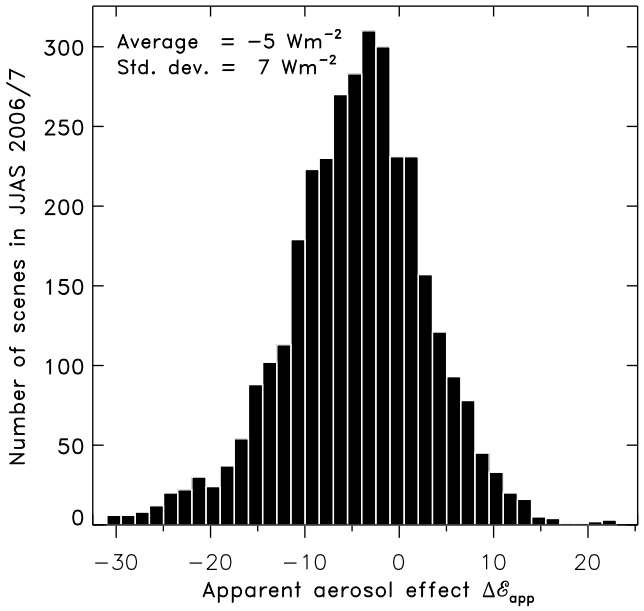

Figure 7. Frequency distribution of the apparent aerosol effect $\Delta\mathcal{E}_{app}$ of all aerosol-unpolluted marine water cloud scenes over the South Atlantic Ocean between 20°S and 10°N, and 10°W and 20°E, in June, July, August, and September of 2006 and 2007, with AAI < 0, CF > 0.3 and CP > 700 hPa. A total number of 3358 pixels (0.25 s IT) satisfying these conditions were found. The mean apparent aerosol effect $\overline{\Delta\mathcal{E}_{app}} = -5$ Wm^{-2} and the standard deviation $\sigma = 7$ Wm^{-2}.

CALIOP 1064 nm backscatter signal shown in Figure 5 was acquired during the daytime, which is noisier than the nighttime signal, but it is separated in time only four hours from the Envisat overpass. It shows the strongly reflecting cloud layer at around 0.5 km altitude and the vertically extensive smoke layer between about 0.5 and 4 km altitude. The red arrow indicates the location of the white dot in Figure 4, where the AAI reaches the high value of 3.8. Clearly, clouds are overlain by absorbing aerosols, causing the high AAI value and the strong aerosol DRE at this point.

6. Accuracy Assessment

[42] The uncertainties of the algorithm will be analyzed in this section. More particularly, the error ϵ in equation (7) will be specified.

6.1. Unpolluted Cloud Spectra Accuracy Assessment

[43] The most important error source in equation (7) is the modeling of the unpolluted cloud spectra, expressed by the uncertainty of the reflectance difference. This term can be estimated directly by comparing modeled and measured unpolluted reflectance spectra. One example of a modeled and a measured unpolluted cloud reflectance spectrum is shown in Figure 6. The measured cloud reflectance spectrum on 14 August 2006 at 10:30:03.73 UTC over the South Atlantic Ocean is shown in black. The absence of UV-absorbing aerosols was confirmed by the negative AAI value of −0.8. The FRESCO cloud fraction and cloud pressure were 0.7 and 856 hPa, respectively, for this scene, indicating a marine low level cloud. The cloud optical thickness and droplet effective radius for this scene were 14.3 and 15.4 μm, respectively. The simulated unpolluted cloud reflectance spectrum using these parameters is shown in orange. The difference between the simulated and measured reflectance spectra is plotted in the lower panel of Figure 6, and shows that the difference is in general very small (<0.015) for this scene. The differences are well within the uncertainty of SCIAMACHY's reflectance measurements of about 3%. Apparently, an unpolluted cloud reflectance spectrum can be accurately extrapolated from the SWIR to the visible and the UV.

[44] The differences between the modeled and measured spectra are caused by SCIAMACHY's measurement uncertainty and the errors in the retrieval of the cloud optical thickness and effective droplet size. Minor causes are interpolation errors in the LUT and possibly scattering by aerosols in the scene that cannot be distinguished from clouds. The latter errors are random, but SCIAMACHY measurement and τ_{cld} and r_{eff} retrieval errors may be systematic. To quantify the random and systematic errors, an apparent aerosol effect $\Delta\mathcal{E}_{app}$ can be defined for aerosol-unpolluted clouds as the apparent radiative forcing arising from measurement uncertainties. $\Delta\mathcal{E}_{app}$ is ideally zero for an unpolluted cloud scene, but was −5 Wm^{-2} for this scene.

[45] The apparent aerosol effect $\Delta\mathcal{E}_{app}$ was determined for all aerosol-unpolluted marine cloud scenes in June - September of 2006 and 2007 over the South Atlantic Ocean between 20°S and 10°N and 10°W and 20°E. All ocean scenes with AAI < 0, FRESCO CF > 0.3, CP > 700 hPa and CPI < 5 were processed, to ensure the scenes contained aerosol-unpolluted low level marine water clouds. The frequency distribution of $\Delta\mathcal{E}_{app}$ (Figure 7) shows the range of $\Delta\mathcal{E}_{app}$ from about −30 to +20 Wm^{-2}, with an average of −5 Wm^{-2} and a standard deviation of 7 Wm^{-2}. The average $\overline{\Delta\mathcal{E}_{app}}$ of −5 Wm^{-2} represents the systematic error from both the SCIAMACHY measurement uncertainty and the uncertainty in the retrieval of the cloud optical thickness and cloud effective droplet size, which causes an offset of the modeled reflectance spectrum. Therefore, in this paper, the aerosol DRE over clouds was corrected for this bias: $\Delta\mathcal{E}_{aer}^{corr} = \Delta\mathcal{E}_{aer} - \overline{\Delta\mathcal{E}_{app}}$. The standard deviation σ of 7 Wm^{-2} represents the random error in the reflectance difference, which is taken as the uncertainty of this term.

6.2. Polluted Cloud Scene

[46] In order to estimate the errors of the various assumptions in the algorithm, the aerosol-polluted cloud scene was also modeled using the RTM. The simulation of the cloud case was repeated, but with an aerosol layer added to the model. A previous attempt to model a similar case with UV-absorbing aerosols overlying a cloud was unsuccessful in simulating the strong reduction of reflectance in the UV [*De Graaf et al.*, 2007]. The main reason was the use of an aerosol model with a wavelength independent refractive index ('gray' aerosol), representative of black carbon (BC). Recent studies have indicated that biomass burning aerosols are characterized by a significant fraction of organic carbon (OC) [e.g., *Kirchstetter et al.*, 2004; *Bergstrom et al.*, 2007], which is produced mainly by incomplete combustion processes. In contrast to BC, the light absorbing efficiency

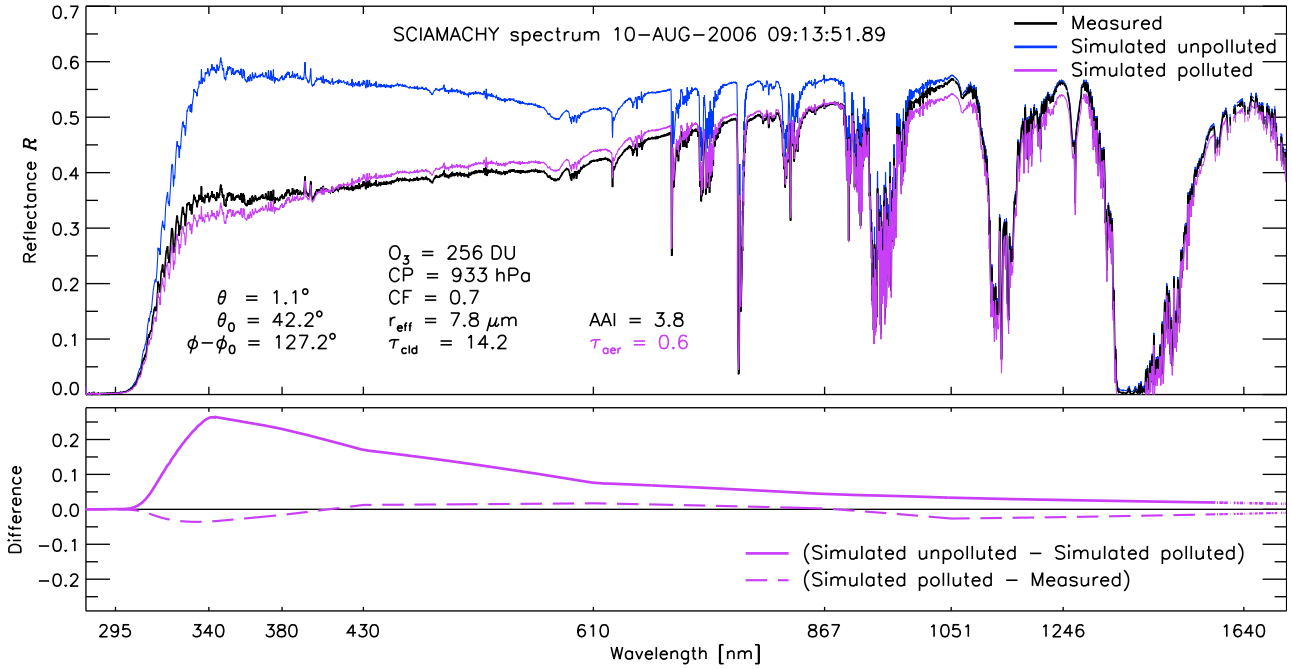

Figure 8. (top) Modeled aerosol-polluted cloud reflectance spectrum (purple), together with the measured SCIAMACHY scene reflectance (black) and the modeled equivalent aerosol-unpolluted cloud reflectance spectrum (blue) on 10 August 2006 at 09:13:51.89 UTC. (cf. Figure 2 and the black rectangle in Figure 4. The cloud and scene parameters are the same as in Figure 2.) The optical thickness of the model aerosol layer τ_{aer} was 0.6 at 550 nm. (bottom) Difference between the simulated and measured aerosol-polluted cloud reflectance spectra (dashed purple) and the difference between the simulated unpolluted and polluted cloud reflectance spectra (solid purple).

of OC increases strongly with decreasing wavelength in the UV. The wavelength dependence of the aerosol absorption is expressed by the absorption Ångström exponent, which is different for different types of aerosols. The absorption Ångström exponent for African biomass burning aerosols from SAFARI 2000 observations was found to be around 1.45 in the spectral region from 325 to 1000 nm [*Bergstrom et al.*, 2007; *Russell et al.*, 2010]. Satellite observations from OMI proved better fitted with aerosol models that had absorption Ångström exponents from 2.5 to 3 in the UV [*Jethva and Torres*, 2011].

[47] For the scene in Figure 2, a Mie model for smoke was created, using a refractive index at 550 nm of $1.54 - 0.018i$. This number was found for aged smoke during the SAFARI 2000 campaign [*Haywood et al.*, 2003] and was used for all wavelengths longer than 550 nm. However, for the UV spectral region the imaginary refractive index was modified so that the absorption Ångström exponent was 2.91 in the UV, which fits the wavelength dependence of the reflectance spectrum well. A bi-modal lognormal size distribution model was used, based on the 'very aged' (5 days) biomass plume found over Ascension Island during SAFARI 2000 [*Haywood et al.*, 2003]. The geometric radii for this haze plume used in the simulations here were $r_c = 0.255\ \mu$m and $r_f = 0.117\ \mu$m for the coarse and fine modes, with standard deviations $\sigma_c = 1.4$ and $\sigma_f = 1.25$, respectively. The fine mode number fraction was 0.9997.

[48] A layer of this aerosol model was placed between 1 and 4 km altitude, above the cloud layer. The aerosol extinction optical thickness τ_{aer} of the aerosol layer was fitted so that the total irradiance change of the modeled scene matched that of the measured scene. This yielded a τ_{aer} of 0.6 at 550 nm. The reflectance spectrum of this modeled scene is shown by the purple curve in Figure 8, while the measured (black) and modeled unpolluted (blue) cloud reflectance spectra are given for reference. The differences between the modeled aerosol-polluted cloud scene and the measured and modeled unpolluted cloud scenes are given in Figure 8 (bottom). The simulation follows the measurements closely over most of the spectral region, confirming the wavelength dependence of the smoke refractive index. Below about 400 nm the slope of the reflectance spectrum is slightly overestimated, so the absorption Ångström exponent should probably be smaller in this spectral region for this scene. However, there is no reason for the absorption Ångström exponent to be constant over any spectral region [*Bergstrom et al.*, 2007]. The assessment of the correct aerosol microphysical properties from measurements is dependent on many variables for every scene. Furthermore, the correct estimate of these aerosol parameters is exactly what is avoided when the actual spectral reflectance measurements are taken instead of a modeled aerosol layer. For the error estimates, derived below, the current model will be assumed representative for the smoke in the measured scenes.

6.2.1. Anisotropy Factor

[49] From the model results the anisotropy factor of the aerosol-polluted cloud scene $B_{cld+aer}$ can now be determined for any geometry. For the scene shown in Figure 8 the anisotropy factor of the aerosol-polluted scene is slightly different from that of the aerosol-unpolluted cloud scene, see

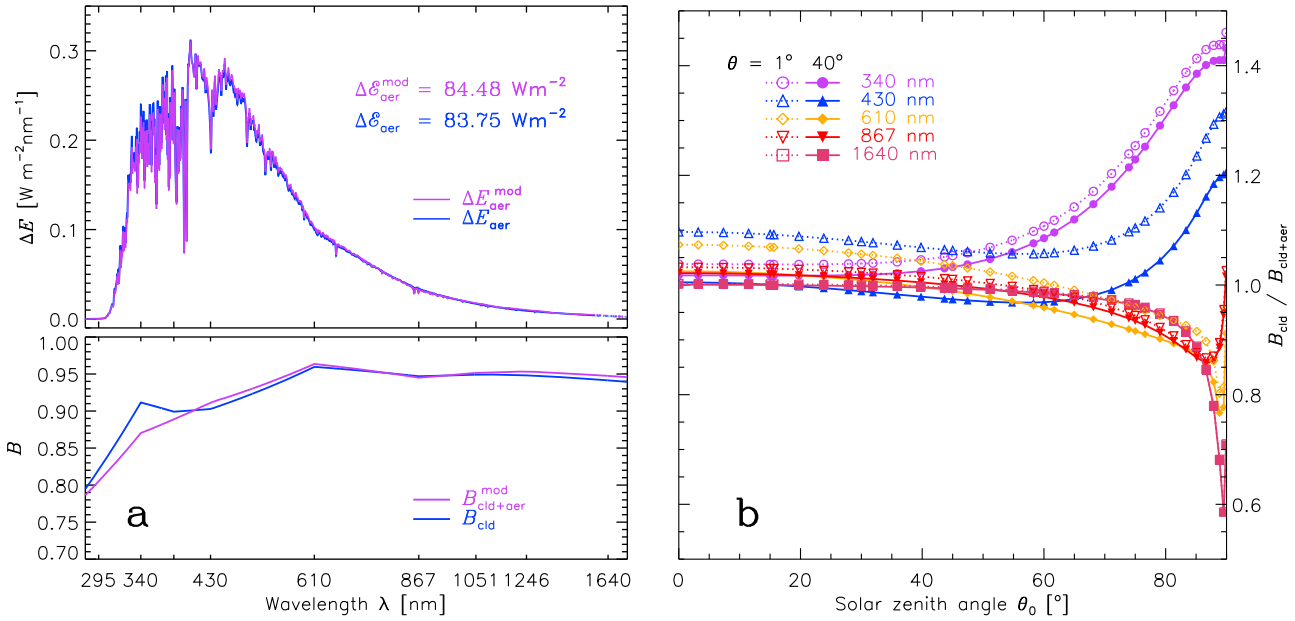

Figure 9. Changes in the anisotropy factor due to aerosols in the scene. (a) (top) Net irradiance change (absorbed energy) as a function of wavelength for the scene indicated by the black rectangle in Figure 4 using the modeled aerosol-polluted cloud reflectance spectrum as shown in Figure 8. The blue curve shows the irradiance change using the anisotropy factor of the modeled aerosol-unpolluted cloud scene B_{cld} as in equation (7), while the purple curve shows the irradiance change with the actual (modeled) aerosol-polluted cloud scene anisotropy. (bottom) Anisotropy factor for the modeled unpolluted cloud scene B_{cld} (blue) and the modeled polluted cloud scene $B_{cld+aer}$ (purple). (b) Anisotropy change as a function of solar zenith angle for selected wavelengths due to the presence of the aerosols. The modeled scene was the same as in Figure 9a and Figure 8. The dotted lines with open symbols show the anisotropy change for a viewing zenith angle of 1°. The solid line with filled symbols shows the anisotropy change for a viewing zenith angle of 40°.

Figure 9a. As mentioned above, the optical thickness of the aerosol layer τ_{aer} was fitted so that the aerosol DRE, using equation (7), was the same for the modeled aerosol-polluted cloud scene as for the measured scene (84 Wm^{-2}). When the actual anisotropy factor of the modeled aerosol-polluted cloud scene was used, as in equation (6), the aerosol absorption shifts slightly from the UV to more visible wavelengths (see top panel in Figure 9a). Since the peak of the solar irradiance is in the visible, the total aerosol DRE increased by 0.9% (from 83.75 to 84.48 Wm^{-2}).

[50] A modeling study showed that the angular redistribution of scattered radiation by aerosols is dependent on τ_{aer}, wavelength and geometry. The dependence on τ_{aer} is linear, with an increasing change for increasing τ_{aer}. The change in anisotropy as a function of solar zenith angle is given in Figure 9b for several wavelengths. It is relatively small at any wavelength and viewing zenith angle for solar zenith angles below 60°. For larger solar zenith angles the change can be larger. Therefore, the error due to the anisotropy factor assumption is estimated to be about 1–2 Wm^{-2}.

6.2.2. Residual Aerosol Optical Thickness

[51] The most important assumption in the method is the assumption that the cloud parameters r_{eff} and τ_{cld} can be directly retrieved from the SWIR part of the reflectance spectrum. A residual aerosol absorption optical thickness τ_{aer} will offset the retrieved cloud parameters, which could even be erroneously interpreted as an indirect aerosol effect [*Haywood et al.*, 2004]. Here, a lower τ_{cld} from residual τ_{aer} in the scene will result in a lower retrieved reflectance over the entire spectral range, which will result in an underestimation of the aerosol DRE.

[52] For the case shown in Figure 8, the optical thickness of the modeled aerosol layer τ_{aer} was 0.046 at 1246 nm, resulting in some residual absorption. To estimate the error in the retrieved aerosol effect, the residual aerosol extinction optical thickness τ_{aer} at 1246 nm, which represents both absorption and scattering, was added to τ_{cld} before the cloud reflectance spectrum was read from the LUT. This resulted in a higher reflectance and a 1.2%, or about 1 Wm^{-2}, increase of the aerosol DRE. This effect is proportional to τ_{aer}. Consequently, the aerosol DRE is underestimated at higher values.

6.2.3. FRESCO Retrievals

[53] A layer of the smoke model described above was placed over a modeled cloud layer to assess the changes in FRESCO retrievals due to aerosol absorption. A water cloud with optical thickness of 20 was placed in a layer between 1 and 2 km, the smoke layer was placed between 4 and 5 km with varying τ_{aer}. The change in FRESCO CP and FRESCO CF for increasing τ_{aer} is shown in Figure 10. FRESCO CF is increasingly affected by aerosol absorption, while FRESCO CP is affected only for τ_{aer} larger than about 1.5 at 550 nm. Note that the AAI for an τ_{aer} of 1.5 at 550 nm is already as high as 9.

[54] Since the maximum τ_{aer} for smoke over the South Atlantic Ocean is about 1.5 at 532 nm [*Chand et al.*, 2009], the

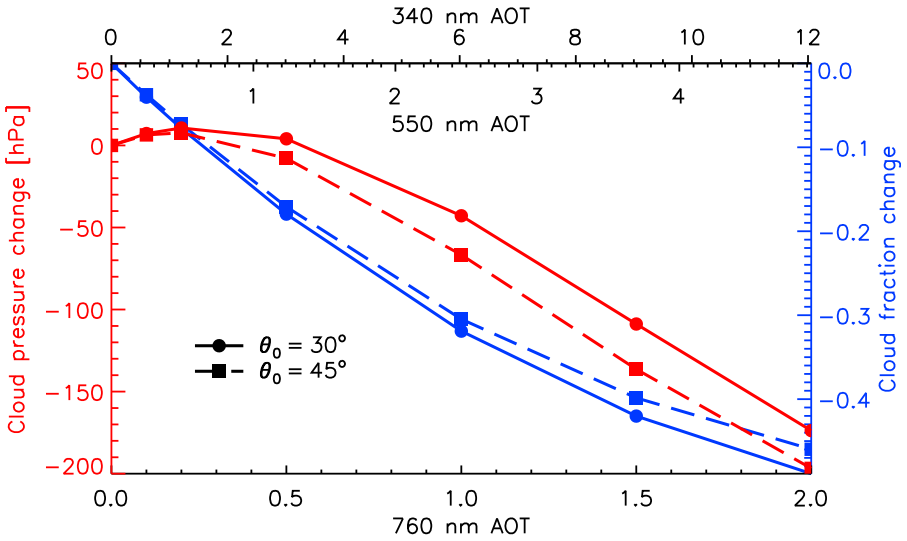

Figure 10. Change of FRESCO cloud pressure (red) and cloud fraction (blue) retrievals, for increasing aerosol load above a cloud at two solar zenith angles and nadir view. The x-axes show the τ_{aer} of the smoke layer at three different wavelengths. The water cloud, with a cloud optical thickness of 20, was placed between 1 and 2 km, while the absorbing smoke layer was placed between 4 and 5 km.

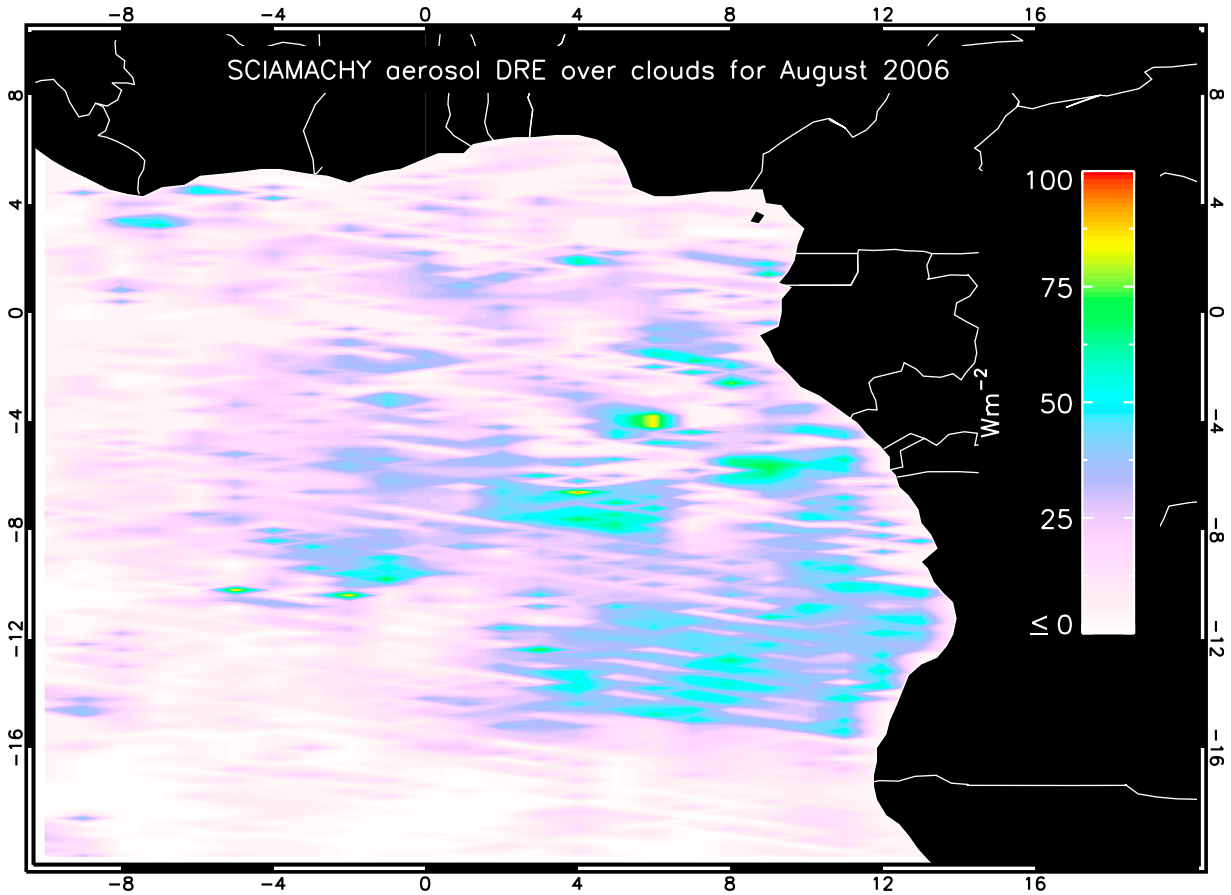

Figure 11. Monthly averaged aerosol DRE over marine clouds (CF > 0.3, CP > 700 hPa, CPI < 5) measured by SCIAMACHY in August 2006 over the South Atlantic Ocean between 20°S and 10°N and 10°W and 20°E. Note that complete spatial coverage of SCIAMACHY nadir measurements is only once per six days. Therefore, grid box values are averages of about 4–5 SCIAMACHY measurements.

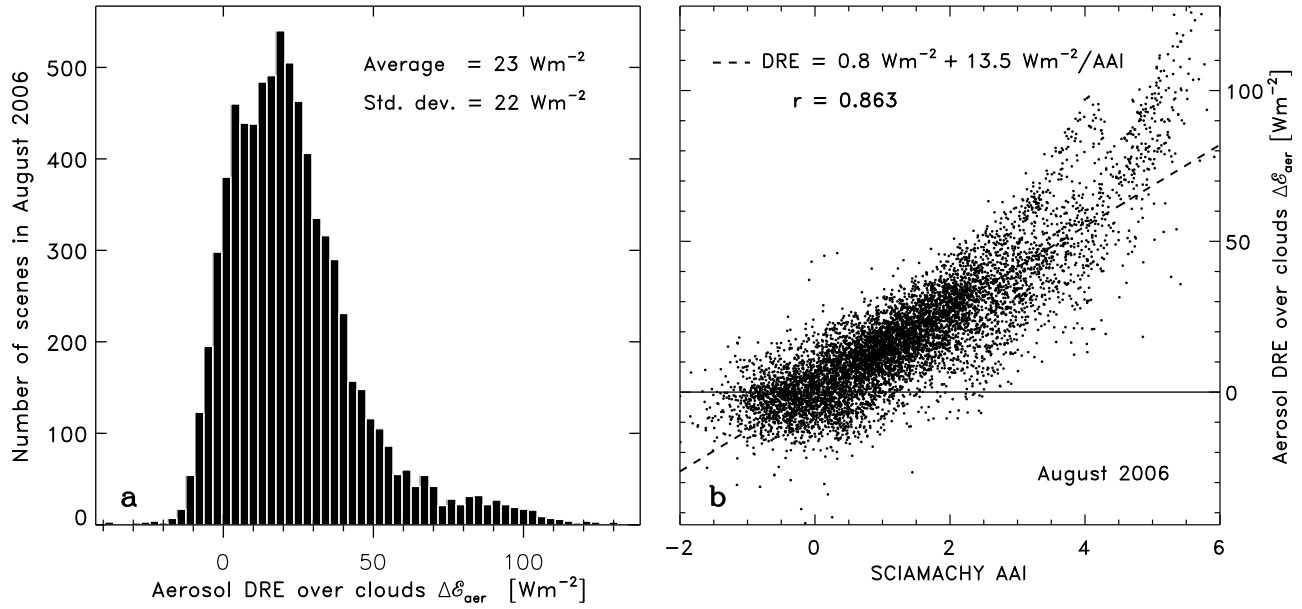

Figure 12. (a) Frequency distribution of all aerosol DRE retrievals over marine clouds (CF > 0.3, CP > 700 hPa, CPI < 5) in August 2006 in the area shown in Figure 11. All SCIAMACHY 0.25 s pixels satisfying these conditions were processed. (b) Aerosol DRE over clouds as a function of AAI for the data points of Figure 12a. The dashed line shows the linear least squares fit of the aerosol DRE and AAI, with an offset of 0.8 Wm^{-2} and a slope of 13.5 Wm^{-2} · AAI^{-1}. Pearson's correlation coefficient r was 0.863.

influence of aerosol absorption on the FRESCO CP retrieval is expected to be small. Furthermore, since cloud height has a small influence on the aerosol DRE (section 4.2), the error from FRESCO CP retrieval uncertainties can be neglected.

[55] The FRESCO CF is underestimated by about 0.2 for an τ_{aer} of 1.5 at 550 nm. This can change the mean apparent aerosol effect $\Delta\mathcal{E}_{app}$ for polluted scenes, since the filtering on CF can be changed. The potential error for this effect was investigated by changing the CF filter for the unpolluted cases from CF > 0.3, which is used to ensure the presence of clouds in the scene (see section 6.1), to the maximum expected change of CF > 0.5. This changed the mean $\Delta\mathcal{E}_{app}$ by 1.1 Wm^{-2} on average.

6.3. Total Error

[56] By considering the selected aerosol-polluted cloud scene representative for the algorithm, the total error ϵ for the aerosol DRE over clouds can found by adding the relative error estimates above. The error of a miscalculation of the mean $\Delta\mathcal{E}_{app}$ due to changes in FRESCO CF is also treated as a random error. The error in the aerosol DRE due to possible variations in the additional input parameters, as a result of the presence of an aerosol layer, is estimated to be less than 1 Wm^{-2} over oceans. Then the total error in the aerosol DRE over clouds from SCIAMACHY ocean scenes is estimated at 8 Wm^{-2}.

7. Regional Monthly Averaged Aerosol DRE Over Clouds

[57] The regionally averaged aerosol DRE over marine clouds was determined over the South Atlantic Ocean between 20°S – 10°N and 10°W – 20°E in August 2006, see Figure 11. In this month a period of strong biomass burning was observed from about 10–21 August. Only water cloud scenes were averaged. Clear-sky scenes and scenes with ice clouds were discarded, by allowing only scenes with cloud fraction higher than 0.3, cloud pressures higher than 700 hPa and cloud phase index below 5. No selection on aerosol amount was made. Figure 11 shows variations in the aerosol DRE over clouds, which has never been shown before using actual measurements. Some of the structures are caused by the low sampling of SCIAMACHY (see section 3.1), but most is due to the variable cloud and aerosol fields, which change rapidly in days and even within one day.

[58] The frequency distribution of the aerosol DRE over clouds in this area in August 2006 is given in Figure 12a. The statistics from Figure 12a are slightly different from Figure 11, because pixel-by-pixel values are used here, while the values in Figure 11 are grid box averaged values. Figure 12 shows that the maximum DRE over clouds in a SCIAMACHY pixel in August 2006 was 132 ± 8 Wm^{-2}, and the regionally and monthly average of the aerosol DRE over clouds in August was 23 ± 8 Wm^{-2} with a standard deviation during this month of 22 Wm^{-2}.

[59] The relationship between the AAI and the aerosol DRE over clouds for the same data shown in Figure 12a is plotted in Figure 12b. It is linear, except for higher values of aerosol DRE. This means that the AAI, combined with cloud fraction values, is a good proxy for the aerosol DRE over clouds from a satellite perspective [e.g., *Wilcox*, 2012; *Peters et al.*, 2011]. A linear least squares fit yielded a slope of 13.5 Wm^{-2} per unit AAI. Some of the spread of aerosol DRE as a function of AAI may be due to the variability of the AAI as a function of geometry and aerosol layer height, which influence the absolute AAI value. The deviation from the linear fit at higher DRE is unclear, especially since aerosol DRE over clouds is probably underestimated for

high values. The AAI is likely non-linear with the amount of aerosols or aerosol absorption optical thickness for higher AAI values.

8. Conclusions

[60] A new method was introduced to retrieve the aerosol DRE over clouds using space-based spectrometer measurements and RTM results of cloud scene TOA reflectances. In order to avoid the difficulties in retrieving aerosol parameters from satellite instruments in general, and in cloudy scenes in particular, only cloud parameters are retrieved from the measurements, along with scene parameters that are needed to characterize the cloud reflectance spectrum. The latter include generally available parameters like scattering geometry, total ozone column and surface albedo. In this paper, only ocean scenes are considered and the spectral surface albedo for all scenes is assumed to be low. Cloud fraction and cloud height can be retrieved from well-established retrieval methods. The FRESCO algorithm was used here, which is relatively unaffected by aerosol contamination. Cloud droplet effective radius r_{eff} and cloud optical thickness τ_{cld} can be retrieved in the SWIR with also well-established algorithms used for MODIS and SEVIRI, among others. However, special care must be taken when retrieving these parameters in aerosol contaminated cloud scenes. Absorption by aerosols in the cloud retrieval bands can bias the retrieved cloud parameters, which is relevant in the current context. Therefore, the cloud parameters are retrieved as far in the SWIR as possible, where the aerosol extinction optical thickness τ_{aer} becomes negligible.

[61] All the aerosol DRE values presented in this paper were retrieved using the 1246/1640 nm wavelength pair to estimate cloud parameters r_{eff} and τ_{cld}. In cases with high aerosol extinction optical thickness this will cause an underestimation of the aerosol DRE over clouds. The case presented in this paper was fitted with an aerosol layer, with $\tau_{\mathrm{aer}} = 0.6$ at 550 nm, which may have caused an underestimation of about 1.2% of the retrieved aerosol DRE of 84 Wm^{-2}. This error increases with increasing τ_{aer}, which can be as high as 1.5 for elevated aerosol layers [*Chand et al.*, 2009]. Therefore the use of reflectances at even longer wavelengths in the SWIR, if available, would be helpful to reduce this error, because aerosols attenuate the radiation most efficiently at wavelengths comparable to their own sizes. This means that a retrieval of r_{eff} and τ_{cld} at wavelengths away from the optically active range of the aerosols will be optimal.

[62] With the retrieved cloud and scene parameters a reflectance spectrum can be simulated for an aerosol-unpolluted cloud scene. This reflectance spectrum can be compared with the measured reflectance and the aerosol DRE can be determined for any water cloud scene for which the reflectance spectrum is measured in the solar spectral range, while aerosol microphysical property assumptions and retrievals are avoided. The differences between the spectra can be attributed directly to aerosol absorption, although scattering effects may also remove or add radiation in the viewing direction. The latter effect is indicated by the change in the anisotropy factor B, which is small compared to the reduction in the reflectance due to absorption, for smoke.

[63] The aerosol DRE over clouds from SCIAMACHY was averaged for all cloudy scenes in a box over the South Atlantic Ocean in August 2006. During this period an extensive biomass burning aerosol plume was advected from the African mainland over a permanent marine boundary layer cloud deck. The maximum aerosol DRE found during this period in a single pixel was 132 ± 8 Wm^{-2}. Such high values were also found in the reduction of shortwave flux from CERES in areas with high TOMS AI near China [*Hsu et al.*, 2003]. The regionally and monthly averaged aerosol DRE over clouds in August 2006 was 23 ± 8 Wm^{-2} with a variation over the region in this month of 22 Wm^{-2}.

[64] The relationship between aerosol DRE over clouds and simultaneously derived AAI was found to be mostly linear: $\Delta\mathcal{E}_{\mathrm{aer}} = 0.8\ \mathrm{Wm}^{-2} + 13.5 \cdot \mathrm{AAI}^{-1}\ \mathrm{Wm}^{-2}$, with a correlation r of 0.863. This confirms the use of the AAI, combined with cloud fraction, as a proxy for the detection of absorbing aerosols over clouds in statistical studies of semi-direct and indirect effects [e.g., *Wilcox*, 2010, 2012; *Peters et al.*, 2011]. The linearity breaks down for larger values of AAI and aerosol DRE over clouds. It is interesting to note that the aerosol DRE efficiency, i.e. aerosol DRE divided by the aerosol optical thickness ($\mathrm{Wm}^{-2}\tau_{\mathrm{aer}}^{-1}$) is also not a linear function for high τ_{aer} [*Forster et al.*, 2007], although this was found for the aerosol DRE efficiency in clear skies.

[65] SCIAMACHY's 0.25 s pixels have a spatial resolution of approximately 60×30 km^2, and global coverage is reached once every six days. Although with this design SCIAMACHY does not have an optimal spatial resolution, the averaged retrieved aerosol DRE over clouds shows unprecedented details. The aerosol DRE over clouds is dependent on cloud cover and aerosol presence, which are both highly variable. SCIAMACHY has been measuring successfully since mid-2002, which can be used to retrieve time series of the aerosol DRE over clouds and relate this to changes in cloud cover and aerosol presence.

[66] To retrieve the aerosol DRE at an even higher spatial resolution, the method presented here for SCIAMACHY may be used for other instruments as well. For example, MODIS and OMI, flying in the A-Train constellation, may be used to retrieve cloud parameters in the SWIR (from MODIS), while spectral UV reflectance measurements from OMI can be used to determine the aerosol absorption. The spectral range of OMI covers only the wavelength region up to 500 nm, but the current study shows that this will suffice to capture the bulk of the absorbed energy in the solar spectrum. The reflectance spectrum in the visible and SWIR may be estimated using the few reflectance measurements from MODIS at larger wavelengths. With a precomputed cloud reflectance LUT at OMI/MODIS wavelengths the aerosol DRE in cloud scenes may then be estimated at a superior spatial resolution.

[67] The use of retrieved cloud optical thickness and cloud droplet effective radius to construct a (water cloud) reflectance spectrum implies an implicit separation of the aerosol DRE in cloudy scene from that in clear skies. This is one of the areas where observations of aerosol DRE are currently lacking [*Yu et al.*, 2006; *Forster et al.*, 2007]. Consequently, the method presented here can complement studies that

retrieve aerosol parameters in clear-sky only. The latter may be used to derive the aerosol DRE in clear-skies.

[68] In principle, the construction of a modeled aerosol-free and cloud-free reflectance spectrum is also possible, which could be used to compare to a measured cloud-free aerosol scene reflectance spectrum. From this the clear-sky aerosol DRE at the TOA could be directly retrieved from satellite reflectance measurements. The quality of such a retrieval would be highly dependent on the quality of a spectral surface albedo database. In contrast, in cloud covered scenes the surface albedo has only a minor effect on the TOA reflectance spectrum and cloud reflectance spectra are relatively constant. Therefore, this approach for the retrieval of the clear-sky aerosol DRE is probably currently only feasible over the oceans.

[69] **Acknowledgments.** J. F. Meirink is thanked for his help with CPP and his many useful comments. We are indebted to three anonymous reviewers, who helped to improve the manuscript. The work of M.d.G. was funded by the European Space Agency (ESA) within the Support to Science Element, project 22403. The work of L.G.T. was funded by the Netherlands Space Office (NSO) through the SCIA-Visie project.

References

Abel, S. J., H. J. Highwood, J. M. Haywood, and M. A. Stringer (2005), The direct radiative effect of biomass burning aerosols over southern Africa, *Atmos. Chem. Phys.*, *5*, 1165–1211.

Acarreta, J. R., and P. Stammes (2005), Calibration comparison between SCIAMACHY and MERIS onboard ENVISAT, *IEEE Geosci. Remote Sens.*, *2*(1), 31–35.

Acarreta, J. R., P. Stammes, and W. H. Knap (2004), First retrieval of cloud phase from SCIAMACHY spectra around 1.6 μm, *Atmos. Res.*, *72*, 89–105.

Ahmad, Z., P. K. Bhartia, and N. Krotkov (2004), Spectral properties of backscattered UV radiation in cloudy atmospheres, *J. Geophys. Res.*, *109*, D01201, doi:10.1029/2003JD003395.

Anderson, G. P., S. A. Clough, F. X. Kneizys, J. H. Chetwynd, and E. P. Shettle (1986), AFGL atmospheric constituent profiles, *Tech. Rep. AFGL-TR-86-0110*, Air Force Geophys. Lab., Hanscom AFB, Mass.

Bergstrom, R. W., P. Pilewskie, P. B. Russell, J. Redemann, T. C. Bond, P. K. Quinn, and B. Sierau (2007), Spectral absorption properties of atmospheric aerosols, *Atmos. Chem. Phys.*, *7*(23), 5937–5943, doi:10.5194/acp-7-5937-2007.

Bhartia, P. K. (Ed.) (2002), *OMI Algorithm Theoretical Basis Document*, vol. II, *OMI Ozone Products*, 91 pp., NASA Goddard Space Flight Cent., Greenbelt, Md.

Bovensmann, H., J. P. Burrows, M. Buchwitz, J. Frerick, S. Noël, V. V. Rozanov, K. V. Chance, and A. P. H. Goede (1999), SCIAMACHY: Mission objectives and measurement modes, *J. Atmos. Sci.*, *56*(2), 127–150, doi:10.1175/1520-0469.

Bramstedt, K., S. Noël, H. Bovensmann, J. P. Burrows, C. Lerot, L. G. Tilstra, G. Lichtenberg, A. Dehn, and T. Fehr (2009), SCIAMACHY monitoring factors: Observation and end-to-end correction of instrument performance degradation, in *Proceedings of the 2009 Atmospheric Science Conference* [CD-ROM], edited by H. Sawaya-Lacoste, *ESA Spec. Publ. SP-676*, Eur. Space Agency, Frascati, Italy.

Chand, D., T. L. Anderson, R. Wood, R. J. Charlson, Y. Hu, Z. Liu, and M. Vaughan (2008), Quantifying above-cloud aerosol using spaceborne lidar for improved understanding of cloud-sky direct climate forcing, *J. Geophys. Res.*, *113*, D13206, doi:10.1029/2007JD009433.

Chand, D., R. Wood, T. L. Anderson, S. K. Satheesh, and R. J. Charlson (2009), Satellite-derived direct radiative effect of aerosols dependent on cloud cover, *Nat. Geosci.*, *2*, 181–184, doi:10.1038/NGEO437.

Chandrasekhar, S. (1960), *Radiative Transfer*, 393 pp., Dover, Mineola, N. Y.

Coddington, O. M., P. Pilewskie, J. Redemann, S. Platnick, P. B. Russell, K. S. Schmidt, W. J. Gore, J. Livingston, G. Wind, and T. Vukicevic (2010), Examining the impact of overlying aerosols on the retrieval of cloud optical properties from passive remote sensing, *J. Geophys. Res.*, *115*, D10211, doi:10.1029/2009JD012829.

Costantino, L., and F.-M. Bréon (2010), Analysis of aerosol-cloud interaction from multi-sensor satellite observations, *Geophys. Res. Lett.*, *37*, L11801, doi:10.1029/2009GL041828.

De Graaf, M., and P. Stammes (2005), SCIAMACHY Absorbing Aerosol Index: Calibration issues and global results from 2002–2004, *Atmos. Chem. Phys.*, *5*, 3367–3389.

De Graaf, M., P. Stammes, O. Torres, and R. B. A. Koelemeijer (2005), Absorbing Aerosol Index: Sensitivity analysis, application to GOME and comparison with TOMS, *J. Geophys. Res.*, *110*, D01201, doi:10.1029/2004JD005178.

De Graaf, M., P. Stammes, and E. A. A. Aben (2007), Analysis of reflectance spectra of UV-absorbing aerosol scenes measured by SCIAMACHY, *J. Geophys. Res.*, *112*, D02206, doi:10.1029/2006JD007249.

De Haan, J. F., P. B. Bosma, and J. W. Hovenier (1987), The adding method for multiple scattering calculations of polarized light, *Astron. Astrophys.*, *183*, 371–391.

De Rooij, W. A., and C. C. A. H. van der Stap (1984), Expansion of Mie scattering matrices in generalized spherical functions, *Astron. Astrophys.*, *131*, 237–248.

Diner, D. J., et al. (2001), MISR aerosol optical depth retrievals over Southern Africa during the SAFARI-2000 dry season campaign, *Geophys. Res. Lett.*, *28*(6), 3127–3130, doi:10.1029/2001GL013188.

Eskes, H. J., R. J. van der A, E. J. Brinksma, J. P. Veefkind, J. F. de Haan, and P. J. M. Valks (2005), Retrieval and validation of ozone columns derived from measurements of SCIAMACHY on Envisat, *Atmos. Chem. Phys. Discuss.*, *5*, 4429–4475, doi:10.5194/acpd-5-4429-2005.

Forster, P., et al. (2007), Changes in atmospheric constituents and in radiative forcing, in *Climate Change 2007: The Physical Science Basis. Contribution of Working Group I to the Fourth Assessment Report of the Intergovernmental Panel on Climate Change*, edited by S. Solomon et al., pp. 129–234, Cambridge Univ. Press, Cambridge, U. K.

Goloub, P., J.-L. Deuzé, M. Herman, and Y. Fouquart (1994), Analysis of the POLDER polarization measurements performed over cloud covers, *IEEE Trans. Geosci. Remote Sens.*, *32*, 78–88.

Gueymard, C. (2004), The Sun's total and spectral irradiance for solar energy applications and solar radiation models, *Sol. Energy*, *76*, 423–452.

Hansen, J. E. (1971), Multiple scattering of polarized light in planetary atmospheres. Part II. Sunlight reflected by terrestrial water clouds, *J. Atmos. Sci.*, *28*, 1400–1426.

Hauser, A., D. Oesch, N. Foppa, and S. Wunderle (2005), NOAA AVHRR derived aerosol optical depth over land, *J. Geophys. Res.*, *110*, D08204, doi:10.1029/2004JD005439.

Haywood, J., and O. Boucher (2000), Estimates of the direct and indirect radiative forcing due to tropospheric aerosols: A review, *Rev. Geophys.*, *38*(4), 513–543, doi:10.1029/1999RG000078.

Haywood, J. M., S. R. Osborne, P. N. Francis, A. Neil, P. Formenti, M. O. Andreae, and P. H. Kaye (2003), The mean physical and optical properties of regional haze dominated by biomass burning aerosol measured from the C–130 aircraft during SAFARI 2000, *J. Geophys. Res.*, *108*(D13), 8473, doi:10.1029/2002JD002226.

Haywood, J. M., S. R. Osborne, and S. J. Abel (2004), The effect of overlying absorbing aerosol layers on remote sensing retrievals of cloud effective radius and cloud optical depth, *Q. J. R. Meteorol. Soc.*, *130*, 779–800, doi:10.1256/qj.03.100.

Herman, J. R., P. K. Bhartia, O. Torres, C. Hsu, C. Seftor, and E. A. Celarier (1997), Global distributions of UV-absorbing aerosols from NIMBUS 7/TOMS data, *J. Geophys. Res.*, *102*(D14), 16,911–16,922, doi:10.1029/96JD03680.

Hsu, N. C., J. R. Herman, and S. Tsay (2003), Radiative impacts from biomass burning in the presence of clouds during boreal spring in southeast Asia, *Geophys. Res. Lett.*, *30*(5), 1224, doi:10.1029/2002GL016485.

Jethva, H., and O. Torres (2011), Satellite-based evidence of wavelength-dependent aerosol absorption in biomass burning smoke inferred from Ozone Monitoring Instrument, *Atmos. Chem. Phys.*, *11*, 10,541–10,551, doi:10.5194/acp-11-10541-2011.

Johnson, B. T., K. P. Shine, and P. M. Forster (2004), The semi–direct aerosol effect: Impact of absorbing aerosols on marine stratocumulus, *Q. J. R. Meteorol. Soc.*, *130*, 1407–1422, doi:10.1256/qj.03.61.

Jourdan, O., A. A. Kokhanovsky, and J. P. Burrows (2005), Calibration of SCIAMACHY using AATSR top-of-atmosphere reflectance over a hurricane, *IEEE Geosci. Remote Sens. Lett.*, *4*, 8–12, doi:10.1109/LGRS.2006.881726.

Kahn, R., P. Banerjee, D. McDonald, and D. Diner (1998), Sensitivity of multiangle imaging to aerosol optical depth and to pure-particle size distribution and composition over ocean, *J. Geophys. Res.*, *103*(D24), 32,195–32,213, doi:10.1029/98JD01752.

Kawamoto, K., T. Nakajima, and T. Y. Nakajima (2001), A global determination of cloud microphysics with AVHRR remote sensing, *J. Clim.*, *14*(9), 2054–2068, doi:10.1175/1520-0442.

Keil, A., and J. M. Haywood (2003), Solar radiative forcing by biomass burning aerosol particles during SAFARI 2000: A case study based on

measured aerosol and cloud properties, *J. Geophys. Res.*, *108*(D13), 8467, doi:10.1029/2002JD002315.
Kirchstetter, T. W., T. Novakov, and P. V. Hobbs (2004), Evidence that the spectral dependence of light absorption by aerosols is affected by organic carbon, *J. Geophys. Res.*, *109*, D21208, doi:10.1029/2004JD004999.
Knap, W. H., P. Stammes, and R. B. A. Koelemeijer (2002), Cloud thermodynamic-phase determination from near-infrared spectra of reflected sunlight, *J. Atmos. Sci.*, *59*(1), 83–96.
Knobelspiesse, K., B. Cairns, J. Redemann, R. W. Bergstrom, and A. Stohl (2011), Simultaneous retrieval of aerosol and cloud properties during the MILAGRO field campaign, *Atmos. Chem. Phys.*, *11*(13), 6245–6263.
Koelemeijer, R. B. A., J. F. de Haan, and P. Stammes (2003), A database of spectral surface reflectivity in the range 335–772 nm derived from 5.5 years of GOME observations, *J. Geophys. Res.*, *108*(D2), 4070, doi:10.1029/2002JD002429.
Kokhanovsky, A. A., V. V. Rozanov, J. P. Burrows, K.-U. Eichmann, W. Lotz, and M. Vountas (2005), The SCIAMACHY cloud products: Algorithms and examples from ENVISAT, *Adv. Space Res.*, *36*, 789–799, doi:10.1016/j.asr.2005.03.026.
Liou, K. N. (2002), *An Introduction to Atmospheric Radiation*, 583 pp., Academic, San Diego, Calif.
Lohmann, U., and J. Feichter (2005), Global indirect aerosol effects: A review, *Atmos. Chem. Phys.*, *5*, 715–737, doi:10.5194/acp-5-715-2005.
Menzel, W. P., R. A. Frey, B. A. Baum, and H. Zhang (2006), Cloud top properties and cloud phase algorithm theoretical basis document, version 7, report, 55 pp., NASA Goddard Space Flight Cent., Greenbelt, Md. [Available online at http: modis-atmos.gsfc.nasa.gov/MOD06CT:MYD06CT_ATBD_C005.pdf.]
Myhre, G., T. K. Berntsen, J. M. Haywood, J. K. Sundet, B. N. Holben, M. Johnsrud, and F. Stordal (2003), Modeling the solar radiative impact of aerosols from biomass burning during the Southern African Regional Science Initiative (SAFARI-2000) experiment, *J. Geophys. Res.*, *108*(D13), 8501, doi:10.1029/2002JD002313.
Nakajima, T., and M. D. King (1990), Determination of the optical thickness and effective particle radius of clouds from reflected solar radiation measurements: Part I: Theory, *J. Atmos. Sci.*, *47*(15), 1878–1893.
Noël, S., K. Bramstedt, H. Bovensmann, J. P. Burrows, M. Gottwald, and E. Krieg (2007), SCIAMACHY degradation monitoring results, in *Proceedings of the 2007 Envisat Symposium* [CD-ROM], edited by H. Lacoste and L. Ouwehand, *ESA Spec. Publ. SP-636*, Eur. Space Agency, Frascati, Italy.
Peters, K., J. Quaas, and N. Bellouin (2011), Effects of absorbing aerosols in cloudy skies: A satellite study over the Atlantic Ocean, *Atmos. Chem. Phys.*, *11*, 1393–1404, doi:10.5194/acp-11-1393-2011.
Platnick, S., M. D. King, S. A. Ackerman, W. P. Menzel, B. A. Baum, J. C. Riédi, and R. A. Frey (2003), The MODIS cloud products: Algorithms and examples From Terra, *IEEE Trans. Geosci. Remote Sens.*, *41*(2), 459–473.
Rast, M., and J. L. Bezy (1999), The ESA Medium Resolution Imaging Spectrometer MERIS: A review of the instrument and its mission, *Int. J. Remote Sens.*, *20*(9), 1681–1702.
Redemann, J., Q. Zhang, P. B. Russel, J. M. Livingston, and L. A. Remer (2009), Case studies of aerosol remote sensing in the vicinity of clouds, *J. Geophys. Res.*, *114*, D06209, doi:10.1029/2008JD010774.
Remer, L. A., et al. (2005), The MODIS aerosol algorithm, products and validation, *J. Atmos. Sci.*, *62*, 947–973, doi:10.1175/JAS3385.1.
Roebeling, R. A., A. J. Feijt, and P. Stammes (2006), Cloud property retrievals for climate monitoring: Implications of differences between Spinning Enhanced Visible and Infrared Imager (SEVIRI) on METEOSAT-8 and Advanced Very High Resolution Radiometer (AVHRR) on NOAA-17, *J. Geophys. Res.*, *111*, D20210, doi:10.1029/2005JD006990.
Russell, P. B., et al. (2010), Absorption Angstrom exponent in AERONET and related data as an indicator of aerosol composition, *Atmos. Chem. Phys.*, *10*(3), 1155–1169, doi:10.5194/acp-10-1155-2010.
Sakaeda, N., R. Wood, and P. J. Rasch (2011), Direct and semidirect aerosol effects of southern African biomass aerosol, *J. Geophys. Res.*, *116*, D12205, doi:10.1029/2010JD015540.
Stammes, P. (2001), Spectral radiance modelling in the UV-visible range, in *IRS 2000: Current Problems in Atmospheric Radiation*, edited by W. Smith and Y. Timofeyev, pp. 385–388, A. Deepak, Hampton, Va.
Stammes, P., L. G. Tilstra, R. Braak, M. de Graaf, and E. A. A. Aben (2008), Estimate of solar radiative forcing by polluted clouds using OMI and SCIAMACHY satellite data, in *Proceedings of the International Radiation Symposium (IRS2008)*, edited by T. Nakajima and M. Akemi Yamasoe, pp. 577–580, Am. Inst. of Phys. Press, College Park, Md.
Stephens, G. L., et al. (2002), The CloudSat mission and the A-Train, *Bull. Am. Meteorol. Soc.*, *83*, 1771–1790, doi:10.1175/BAMS-83-12-1771.
Swap, R. J., M. Garstang, S. A. Macko, P. D. Tyson, W. Maenhaut, P. Artaxo, P. Kållberg, and R. Talbot (1996), The long-range transport of southern African aerosols to the tropical South Atlantic, *J. Geophys. Res.*, *101*(D19), 23,777–23,791, doi:10.1029/95JD01049.
Tilstra, L. G., G. van Soest, and P. Stammes (2005), Method for in-flight satellite calibration in the ultraviolet using radiative transfer calculations, with application to Scanning Imaging Absorption Spectrometer for Atmospheric Chartography (SCIAMACHY), *J. Geophys. Res.*, *110*, D18311, doi:10.1029/2005JD005853.
Tilstra, L. G., M. de Graaf, I. Aben, and P. Stammes (2012), In-flight degradation correction of SCIAMACHY UV reflectances and Absorbing Aerosol Index, *J. Geophys. Res.*, *117*, D06209, doi:10.1029/2011JD016957.
Torres, O., P. K. Bhartia, J. R. Herman, Z. Ahmad, and J. Gleason (1998), Derivation of aerosol properties from satellite measurements of backscattered ultraviolet radiation: Theoretical basis, *J. Geophys. Res.*, *103*(D14), 17,099–17,110, doi:10.1029/98JD00900.
Torres, O., P. K. Bhartia, J. R. Herman, A. Sinyuk, P. Ginoux, and B. Holben (2002), A long-term record of aerosol optical depth from TOMS observations and comparison to AERONET measurements, *J. Atmos. Sci.*, *59*(3), 398–413, doi:10.1175/1520-0469.
Torres, O., A. Tanskanen, B. Veihelmann, C. Ahn, R. Braak, P. K. Bhartia, P. Veefkind, and P. Levelt (2007), Aerosols and surface UV products from Ozone Monitoring Instrument observations: An overview, *J. Geophys. Res.*, *112*, D24S47, doi:10.1029/2007JD008809.
Torres, O., H. Jethva, and P. K. Bhartia (2011), Retrieval of aerosol optical depth above clouds from OMI observations: Sensitivity analysis and case studies, *J. Atmos. Sci.*, *69*(3), 1037–1053, doi:10.1175/JAS-D-11-0130.1.
Tummon, F., F. Solmon, C. Liousse, and M. Tadross (2010), Simulation of the direct and semidirect aerosol effects on the southern Africa regional climate during the biomass burning season, *J. Geophys. Res.*, *115*, D19206, doi:10.1029/2009JD013738.
van Soest, G., L. G. Tilstra, and P. Stammes (2005), Large-scale validation of SCIAMACHY reflectance in the ultraviolet, *Atmos. Chem. Phys.*, *5*, 2171–2180, doi:10.5194/acp-5-2171-2005.
Veefkind, J. P., J. F. de Haan, E. J. Brinksma, M. Kroon, and P. F. Levelt (2006), Total ozone from the Ozone Monitoring Instrument (OMI) using the DOAS technique, *IEEE Geosci. Remote Sens.*, *44*(5), 1239–1244.
von Hoyningen-Huene, W., et al. (2007), Validation of SCIAMACHY top-of-atmosphere reflectance for aerosol remote sensing using MERIS L1 data, *Atmos. Chem. Phys.*, *7*, 97–106, doi:10.5194/acp-7-97-2007.
Wang, P., P. Stammes, R. van der A, G. Pinardi, and M. van Roozendael (2008), FRESCO+: An improved O_2 A-band cloud retrieval algorithm for tropospheric trace gas retrievals, *Atmos. Chem. Phys.*, *8*(21), 6565–6576, doi:10.5194/acp-8-6565-2008.
Waquet, F., J. Riedi, L. C. Labonnote, P. Goloub, B. Cairns, J.-L. Deuzé, and D. Tanré (2009), Aerosol remote sensing over clouds using A-Train observations, *J. Atmos. Sci.*, *66*, 2468–2480, doi:10.1175/2009JAS3026.1.
Wilcox, E. M. (2010), Stratocumulus cloud thickening beneath layers of absorbing smoke aerosol, *Atmos. Chem. Phys.*, *10*(23), 11,769–11,777.
Wilcox, E. M. (2012), Direct and semi-direct radiative forcing of smoke aerosols over clouds, *Atmos. Chem. Phys.*, *12*, 139–149, doi:10.5194/acp-12-139-2012.
Winker, D. M., W. H. Hunt, and M. J. McGill (2007), Initial performance assessment of CALIOP, *Geophys. Res. Lett.*, *34*, L19803, doi:10.1029/2007GL030135.
Yu, H., et al. (2006), A review of measurement-based assessments of the aerosol direct radiative effect and forcing, *Atmos. Chem. Phys.*, *6*(3), 613–666, doi:10.5194/acp-6-613-2006.

M. de Graaf, P. Stammes, L. G. Tilstra, and P. Wang, Climate Research and Seismology Department, Royal Netherlands Meteorological Institute, PO Box 201, NL-3730 AE De Bilt, Netherlands. (graafdem@knmi.nl)